POLITECNICO DI TORINO

Master's Thesis in Aerospace engineering

Virtual manufacturing of composite structures with embedded piezoelectric sensors



Supervisors

Zappino Enrico

Petrolo Marco

Candidate

Matteo Barucca

Academic year 2024-2025



Contents

Li	st of	Table	S	V
Li	st of	Figure	es	VI
1	Intr	oducti	ion	1
2	Stat	te of tl	he Art	4
	2.1	Comp	osites	4
		2.1.1	Thermosetting resins	6
		2.1.2	Thermoplastics resins	7
	2.2	Curing	g Process	8
		2.2.1	Manifacturing process and Defects	13
	2.3	SHM	with Embedded Piezoelectric Sensors	14
		2.3.1	Piezoelectrics Materials	16
		2.3.2	Temperature's effect	17
3	Car	rera U	Inified Formulation (CUF)	19
	3.1	One-D	Dimensional Model	20
		3.1.1	Taylor Expansion (TE)	22
		3.1.2	Lagrange Expansion (LE)	24

		3.1.3	Fundamental Nucleus	27
	3.2	Electr	o-Mechanical Model	34
		3.2.1	Capacitance Variation	37
4	Ass	essmer	\mathbf{nt}	41
	4.1	MUL	2 Polito	42
	4.2	Assess	sment 1	44
		4.2.1	Modeling	45
		4.2.2	Displacement u_z along the Length of the Beam \dots	47
		4.2.3	Displacement u_z along the Width of the Beam	50
		4.2.4	Considerations	51
	4.3	Assess	ement 2	53
		4.3.1	Modeling	54
		4.3.2	Analysis through the thickness of a multilayer beam	55
		4.3.3	Considerations	59
	4.4	Assess	ement 3	60
		4.4.1	Actuator	61
		4.4.2	Sensor - Model with elements Q9	64
5	Cap	acitan	ace	70
	5.1	Capac	itance of a free sensor	70
	5.2	Isotro	pic plate with integrated piezoelectric sensor	73
	5.3	Lamin	nated composite with embedded piezoelectric sensor	76
		5.3.1	Capacitance with Permittivity fixed	78
		5.3.2	Capacitance with Permittivity as a function of the Tem-	
			perature	80
		5.3.3	Comparison between PZT-4 and PZT-5A	83

6 Conclusions 90

List of Tables

2.1	Mechanical, piezoelectric, and dielectric properties of PZT-4,	
	PZT-5H, PZT-5A, and PZT-8	16
3.1	Taylor-like polynomials	25
3.2	Coordinates of the points with α_{τ} and β_{τ}	26
4.1	Properties of Aluminum	45
4.2	Maximum Deflection for each type of model	48
4.3	Properties of the Materials	53
4.4	Points A,B,C and D	54
4.5	Stress evaluation at Points A, B, C, displacement w at point D	
	and DOFs	55
4.6	Comparison with Results from the Paper [1]	63
5.1	Properties of Isotropic Material	74
5.2	Material properties for different DOC and temperatures	77
5.3	Capacitance of 4 sensors in free conditions: PZT-4, PZT-5H,	
	PZT-5A and PZT-8	78

List of Figures

2.1	Different type of composite materials	4
2.2	Specific Modulus - Specific Strength	5
2.3	Fases of polimerization	8
2.4	DOC	9
2.5	Shrinkage	10
2.6	Curing cycle	10
2.7	Piezolectric sensors	14
2.8	Piezolectric sensor	15
2.9	Permittivity of PZT-4, PZT-5H, PZT-5A and PZT-8	18
3.1	1D Model	21
3.2	Euler-Bernoulli beam model	22
3.3	Timoshenko beam model	23
3.4	Lagrange Polynomials: L3, L4, L9	25
3.5	Axial approximation (N_i, N_j) , cross-section expansion (F_τ, F_s)	28
3.6	Nodal, Element, and Global stiffness matrices	31
4.1	Codice MUL 2	42
4.2	Modello Assessment 1	44
4.3	LE with 1,2 or 3 Subsections (With L9 elements)	46
4.4	Displacement w [ţm]	47

4.5	Zoom of Displacement w [tm]	48
4.6	Displacement (TE 4)	50
4.7	Displacement (LE with 3 Subsections)	50
4.8	Displacement w along the width[m]	51
4.9	Model Assessment 2	53
4.10	Materials (Blue=1, Red=2)	54
4.11	Section across z-axis	55
4.12	Displacement \mathbf{w}	56
4.13	Displacements \mathbf{v} and \mathbf{u}	56
4.14	Strain ε_{yy} , TE5	57
4.15	Strain ε_{zz} , TE5	57
4.16	Strain ε_{yz} , TE5	57
4.17	Stress σ_{yy} , TE5	58
4.18	Stress σ_{zz} , TE5	58
4.19	Stress σ_{yz} , TE5	58
4.20	Side View	60
4.21	Top View	60
4.22	$Voltage \; [V] . \; . \; . \; . \; . \; . \; . \; . \; . \; .$	61
4.23	E_z	62
4.24	Displacement $w[m]$	62
4.25	Displacement $w(0,y,0)$ and $\sigma_{yy}(0,y,-h/2)$	63
4.26	Displacement w	64
4.27	E_z	65
4.28	Voltage V	65
4.29	Patch Piezoelettrica	65
4.30	E_z	66

4.31	Voltage V	66
4.32	Q4 Element	68
4.33	Displacement w (with element Q4)	68
4.34	E_z	69
4.35	Voltage V	69
5.1	Free sensor subjected to a potential difference	72
5.2	Isotropic plate with embedded piezoeletric system - Plane $\mathbf{x}\mathbf{y}$	73
5.3	Isotropic plate with embedded piezoeletric system - Plane xz	73
5.4	Capacitance as a function of the elastic modulus (isotropic case)	75
5.5	Laminated Composite	76
5.6	Curing Cycle	77
5.7	Piezoeletric Sensor embedded in laminated composite	77
5.8	Capacitance of PZT-4, PZT-5H, PZT-5A and PZT-8 as a function	
	of the Degree of Cure	79
5.9	Capacitance of PZT-4, PZT-5H, PZT-5A and PZT-8 with per-	
	mittivity variable as a function of the Temperature	80
5.10	Zoom of Capacitance of PZT-4, PZT-5H, PZT-5A and PZT-8	
	with permittivity variable as a function of the Temperature	81
5.11	Percentage change calculated with respect to the first real capac-	
	itance value	82
5.12	Comparison of the 3 capacitances: analytical, with fixed permit-	
	tivity and with permittivity as a function of temperature	84
5.13	Percentage change calculated with respect to the first real capac-	
	itance value	85
5.14	Maximum Curing Temperature: 150°C	87
5.15	Maximum Curing Temperature: 165°C	87

5.16	Capacitance trend as a function of DOC in the 3 cases at different	
	maximum curing temperatures	88

Chapter 1

Introduction

The following thesis work is based on the study, through virtual manufacturing, of composite structures with embedded piezoelectric sensors.

Virtual manufacturing is a technique that allows simulating the production processes of a given material and makes it possible to analyze materials and their behavior under certain conditions. This allows for cost reduction and process optimization much faster than would be possible through real-world experiments alone.

Composites usually present different types of defects during or after the manufacturing phase. In this thesis work, an attempt will be made to better analyze them by inserting a piezoelectric sensor inside the composites. This could, however, lead to other issues such as interaction with the tool, shrinkage, a mismatch in the thermal expansion coefficients between the composite material and the piezoelectric element, non-optimal temperature distribution, and other kinds of problems.

The goal, therefore, is to modify the existing MUL2 Polito code, developed at the Politecnico di Torino, to obtain a program capable of simulating this new

scenario, which involves piezoelectric sensors embedded within the composite materials, and can thus be described as a multi-field problem involving the interaction of mechanical stresses and electric fields.

In this thesis work, it is assumed that the piezoelectric sensor is embedded within the composite during the manufacturing process. This could make it possible to monitor what happens inside the composite during the production phase and consequently optimize the curing steps of the composite materials. Furthermore, once the manufacturing phase is complete, the sensor would remain embedded in the composite, providing continuous monitoring even during the operational life, which would significantly improve the maintenance of the composites.

The thesis will begin with a brief description of composite materials and manufacturing processes, focusing on specific types of composites particularly used in the aerospace field. This will be followed by a description of the current state of the art regarding structural health monitoring using piezoelectric materials. Then, the theory behind the MUL2 Polito code will be described, including a brief explanation of the Carrera Unified Formulation (CUF), with a specific focus on one-dimensional models. The next step will be the implementation of the electromechanical part into the code. Subsequently, an assessment chapter will help to become familiar with the code. By studying two different problems—a double-clamped beam and a multilayer beam—a comparison of some results will be presented, using different models proposed by the code. These results will be compared both with analytical solutions and with a case study taken from a scientific paper, in order to demonstrate the validity and effectiveness of the code.

Following this, an electromechanical problem involving a piezoelectric material

is studied. This piezoelectric material, along with a beam of isotropic material, is analyzed for both actuator and sensor applications.

The calculation of the capacitance of a free-standing sensor is then examined, both analytically and directly from the FEM. Subsequently, the variation in capacitance of a sensor integrated into a plate made of isotropic material with a variable elastic modulus is observed.

Finally, the variation in capacitance of a sensor integrated into a 10-layer laminate composite is studied, using the various elastic modulus values assumed by the composite laminate during the manufacturing process as reported in the literature.

Chapter 2

State of the Art

2.1 Composites ¹

A composite material can be described as a combination of two or more materials that, when combined, provide superior properties compared to those of the individual components used separately. The various types of composites are shown in the figure Fig. 2.1:

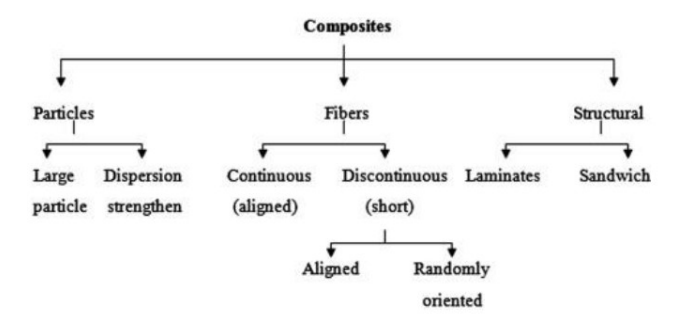


Figure 2.1: Composites 2

 $^{^1}Much$ of the information presented in this section was taken from the course slides [2] and [3]

Composite structures are recognized for their lightness and high mechanical strength (Fig 2.2). Additionally, composites are resistant to corrosion and they have fatigue resistance, excellent fire resistance, and the ability to design the material for optimal performance. This combination makes composite materials ideal for designing high-performance structures intended for specific applications, such as in aeronautics and space.

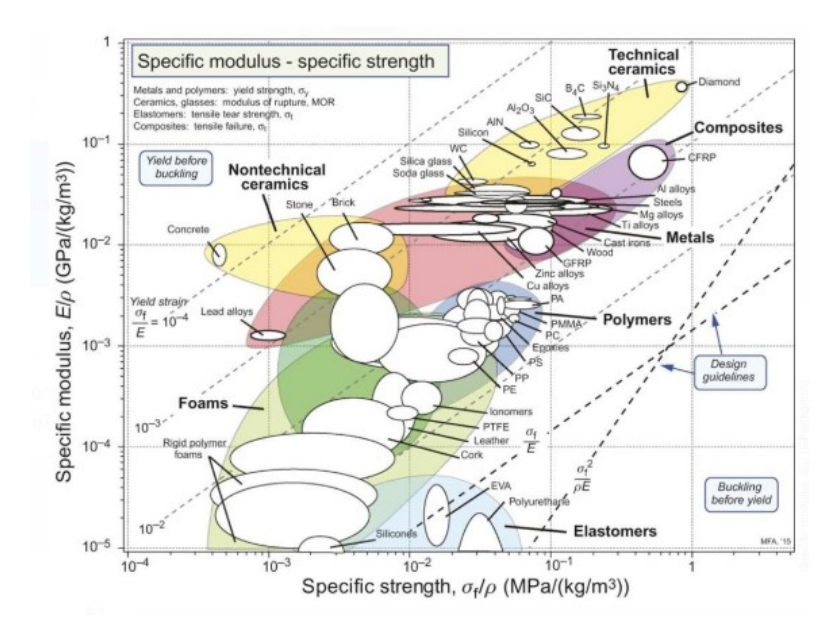


Figure 2.2: Specific Modulus - Specific Strength 3

The **Fiber** is the primary load-carrying element in a composite material. The composite is strong and stiff only in the direction of the fibers. Unidirectional composites exhibit predominant mechanical properties in one direction and are referred to as *anisotropic*, meaning they have mechanical and physical properties that vary with direction relative to the material's natural reference axes. Components made with fiber-reinforced composites can be designed so

²Figure was taken from the course slides [2].

³Figure was taken from the course slides [2].

that the fiber orientation provides optimal mechanical properties, but they can only approximate the truly *isotropic* nature of metals such as aluminum and titanium.

There are many different type of fibers: Carbon fibers are very strong and stiff, used in primary aircraft structures but are expensive and need lightning protection. Glass fibers are cheaper and used in secondary structures like fairings and rotor blades. Kevlar is lightweight and impact-resistant but absorbs moisture and is weak in compression. Ceramic fibers resist very high temperatures, used in turbine blades. Boron fibers are extremely stiff and strong, but expensive, inflexible, and used mainly in military aviation.

Resins are the other fundamental elements in composite materials, as they act as the matrix that holds the reinforcing fibers together. There are different types of resins, each with specific characteristics and applications: Polymer matrix, which is divided into Thermosetting and Thermoplastic types; ceramic matrix; and metal matrix. In this thesis work, the focus will be mainly on composites with polymer resins; therefore, a description of thermosetting and thermoplastic resins will follow.

2.1.1 Thermosetting resins

Thermosetting resins, once cured, cannot be remelted or reshaped.

- Polyimide and phenolic resins have the best thermal properties, but they are brittle and expensive;
- *Polyester resins* are usually combined with glass fibers. They have low mechanical performance, low thermal resistance, but also low cost.
- Epoxy resins are usually combined with carbon fiber; they offer the best

performance and are the most expensive. The curing process is crucial, as will be discussed below;

2.1.2 Thermoplastics resins

Thermoplastics resins are soft and moldable when heated, and solidify upon cooling, a process that can be repeated multiple times without significant degradation. Unlike thermosetting resins, they do not undergo a permanent chemical change during heating.

- Polycarbonate (PC) is a thermoplastic known for its impact resistance and amorphous structure and it has excellent thermal resistance.
- Polyetheretherketone (PEEK) is another high-performance thermoplastic that performs exceptionally well under extreme pressure and temperature conditions. It is characterized by outstanding mechanical properties and excellent thermal and dimensional stability. PEEK offers excellent dielectric properties.
- Polyphenylene Sulfide (PPS) is a thermoplastic known for its ability to resist high temperatures and maintain its integrity under prolonged stress. It exhibits excellent creep resistance and a high elastic modulus, giving it rigidity and mechanical strength.

2.2 Curing Process

The curing process consists of the reticulation of the polymer resin through temperature increase, pressure, and chemical agents. With the curing process is possible to make solid and stable structures with great mechanical properties. During polymerization, thermosetting matrices be subjected to several distinct phases as the chemical reactions progress (Fig. 2.3).

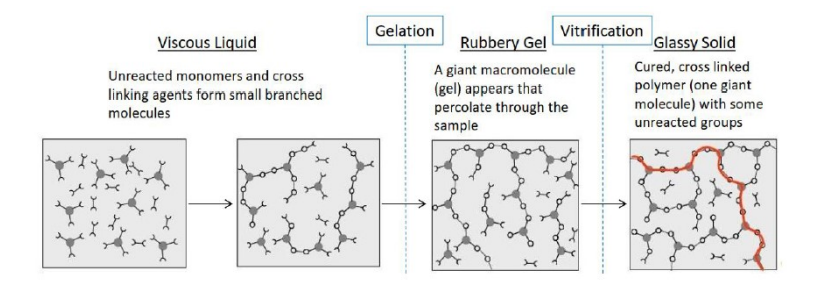


Figure 2.3: Fases of polimerization ⁴

A key parameter in this process is the Degree of Cure (DoC), which indicates the extent of polymerization that is, the formation of chemical bonds within the polymer network. The DoC ranges from 0 to 1 (or 0% to 100%). A value of 1 means the matrix is fully cured and the polymerization process is complete. In practice, most thermosetting matrices reach a DoC of around 90%, which is generally sufficient to achieve the desired material properties.

The higher the Degree of Cure, the better the mechanical properties of the final composite component, such as stiffness, strength, and dimensional stability. The DoC is primarily influenced by two factors: the external temperature and the curing time (Fig. 2.4).

⁴Figure was taken from the course slides [2].

⁵Figure was taken from the course slides [2].

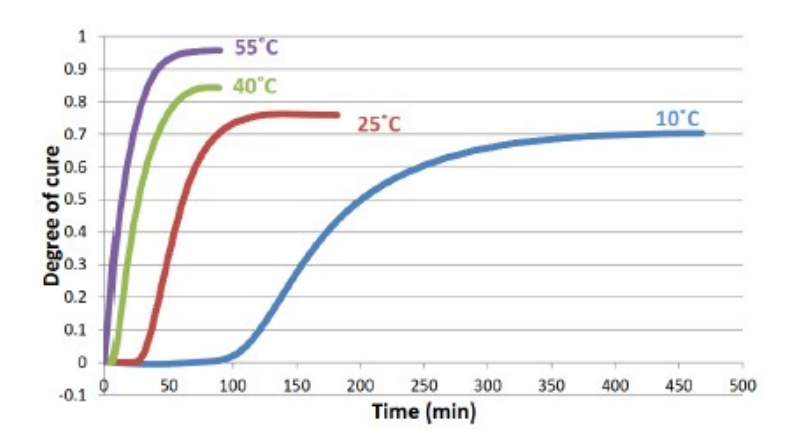


Figure 2.4: DOC ⁵

To accelerate the polymerization process, autoclaves are typically used to increase the temperature, promoting faster and more uniform curing throughout the composite material. During the autoclave processing of thermosetting composite materials, two main objectives are pursued. The first is to eliminate voids and residual gases, thereby improving the compactness of the laminate through the application of vacuum and pressure. The second objective is to promote the chemical reaction between the monomers, transforming them into a three-dimensional, highly cross-linked polymer structure through a polymerization process.

During the curing process, the resin undergoes a reduction in volume, a phenomenon known as shrinkage (Fig. 2.5). This volumetric shrinkage can lead to final deformations in the composite component, potentially compromising its dimensional accuracy and structural integrity. Shrinkage also induces internal stresses within the material, which, if not properly managed, may result in cracking or failure of the component during manufacturing. These internal stresses are especially critical in high-performance applications where precision and reliability are essential.

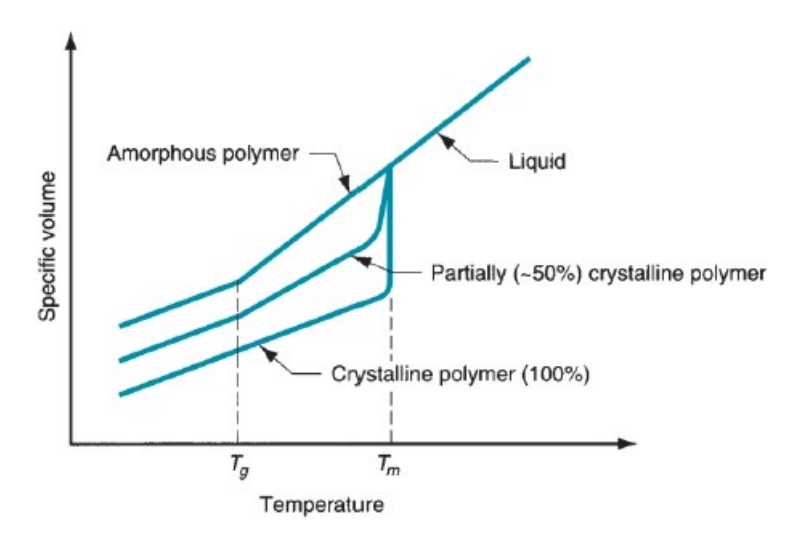


Figure 2.5: Shrinkage 6

For epoxy resins, typical volumetric shrinkage values range from 2% to 8%, depending on the specific formulation and curing conditions. The following images illustrate a typical curing cycle.

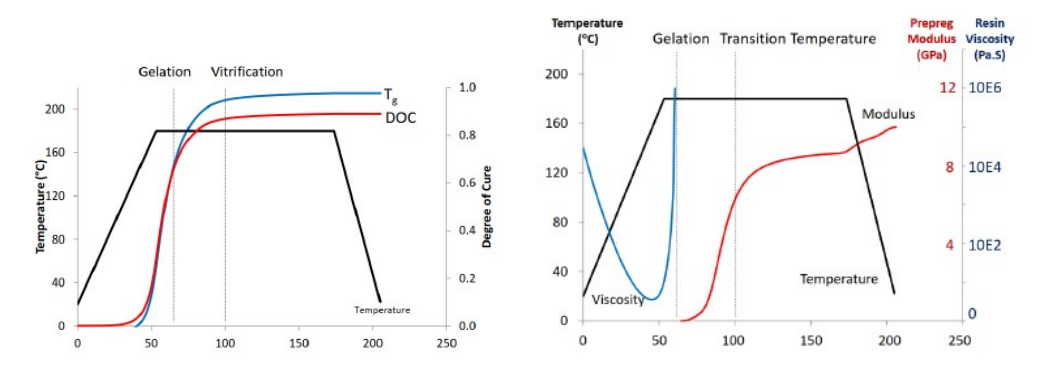


Figure 2.6: Curing cycle 7

The glass transition temperature (T_g) increases progressively with the Degree

⁶Figure was taken from the course slides [2].

⁷Figure was taken from the course slides [2].

of Cure (DoC). The Di Benedetto equation (2.1) make a description of this behavior.

$$\frac{T_g - T_{g_0}}{T_{g_\infty} - T_{g_0}} = \frac{\lambda x}{1 - (1 - \lambda)x}$$
 (2.1)

The process is divided into 3 part:

• At ambient temperature, the resin exhibits high viscosity. As the temperature increases, its viscosity decreases significantly. This behavior is governed by a temperature-dependent relationship that can be described by an Arrhenius-type equation:

$$\mu = Ae^{\frac{\Delta E}{RT}f(x)} \tag{2.2}$$

Viscosity also increases markedly with the Degree of Cure (DoC), particularly near the transition from liquid to solid. In the liquid state, shear stresses are primarily supported by the fiber bed, while normal stresses are shared between the resin—mainly via hydrostatic pressure—and the fiber network. Under autoclave conditions of heat and pressure, the prepreg is compacted and consolidated, facilitating the removal of volatiles and trapped air. A key material parameter that evolves during this process is the fiber volume fraction, which rises as the prepreg thickness decreases during curing. For typical epoxy systems, gelation begins at a DoC between 0.5 and 0.6.

• During gelation, the resin's viscosity increases from a finite value to virtually infinite. At this stage, the resin develops a modulus and begins to behave viscoelastically. It starts to form chemical bonds with the fibers. The emergence of stiffness in the resin, combined with strain mismatches between

resin and fibers, results in the development of *residual stresses*. These stresses are due to differing mechanical responses during the cure.

• As polymerization advances, the glass transition temperature (T_g) also increases. Full transition into the glassy phase typically occurs around $T_g + 25$ °C. Beyond this point, the cure reaction slows considerably, and the increase in modulus becomes more gradual. In a single-step cure cycle, this stage can be divided into two phases: the isothermal hold (soak) period and the cooling stage. The final Degree of Cure usually falls within the range of 0.85 to 0.95.

Curing cycle and temperature profile must be carefully controlled to ensure that the material properties are fully developed throughout the entire structure. Equally important is the fiber orientation, which must precisely follow the specified directions dictated by structural requirements to guarantee optimal mechanical performance. Another key parameter is the fiber volume fraction, which must be consistent across the component to ensure the correct ratio of fiber to resin in every region. Additionally, porosity levels must be minimized, as the presence of voids can significantly degrade the mechanical properties of the composite. Finally, dimensional accuracy, including shape, angularity, and thickness, is essential to ensure that each part fits correctly within the surrounding structure during assembly.

2.2.1 Manifacturing process and Defects

There are three main **Manifacturing Process** for combining resin and fiber:

- Wet processes, where liquid resin is mixed with dry fibers directly within the mold. This method is typically used for processes that allow in-situ impregnation during shaping.
- Liquid Composite Molding (LCM) processes, where dry fiber fabrics are placed into the mold and subsequently infused with resin by applying a pressure gradient, such as in vacuum-assisted resin transfer molding (VARTM).
- *Prepreg processes*, where the resin and fibers are already pre-combined into semi-finished sheets or tapes. These are then laid up onto the tool in the desired orientation and consolidated during the cure cycle.

There are several **Defects** that must be carefully considered during the manufacturing of composite materials. These can be classified into three main categories:

- Deposition and cure defects: delamination, voids, under-cure and improper material deposition;
- Geometrical defects, including disbonding, spring-in, and poor surface finish;
- Post-processing defects, which may arise from machining, assembly, or handling errors.

2.3 SHM with Embedded Piezoelectric Sensors

As just seen, composite materials can exhibit numerous defects both during the manufacturing process and throughout their operational life. To assess their structural integrity, constant Structural Health Monitoring (SHM) is necessary.

In recent years, Non-Destructive Testing (NDT) techniques have been widely used for this purpose [4]. However, these are generally external methods, which often require the structure to be taken out of service.

As explained in paper [5], there has been a growing interest in recent years in the development of in-situ SHM systems. This is made possible by the piezo-electric sensors (Fig. 2.7). It was demonstrated that embedding piezoelectric devices, as opposed to surface mounting, enhances their effectiveness and these sensors are less likely to degrade quickly, as they are protected by the surrounding material [6]. However, this approach often results in a complex stress concentration around the transducer area, leading to improved coupling and greater sensitivity, but at the expense of local structural strength [7]. Sensors integrated directly into the structure would allow for real-time monitoring of the material's health not only during its operational life but also throughout the manufacturing process.

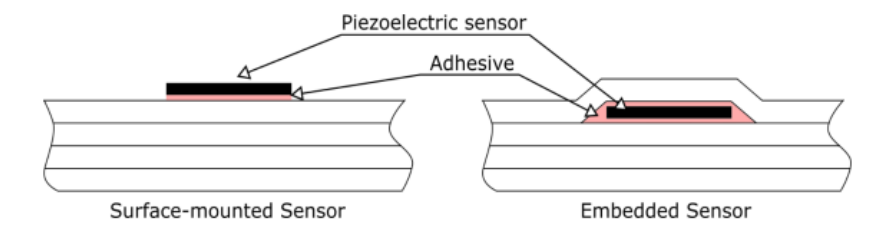


Figure 2.7: Piezolectric sensors ⁸

⁸Figure was taken from the slides [8].

Piezoelectricity is the ability of certain materials to generate an electric field in response to applied mechanical stress or to generate a mechanical stress in response to applied electric field. In the direct mode, microscopic electric dipoles can form within these materials, and their orientation can change depending on the external force applied to them, resulting in the generation of an electric charge [3]. Accurately measuring this electric charge from the integrated piezoelectric sensors could enable continuous and precise monitoring of the composite en- capsulating the piezoelectric sensor. It is a device that converts mechanical stress into electrical charge or voltage (Fig. 2.8), allowing the measurement of pressure, acceleration, or force.

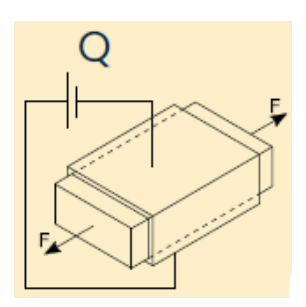


Figure 2.8: Piezolectric sensor ⁹

In according to [8] Piezosensor can be considered a capacitor since it produces a concentration of positive and negative charges on the opposite electrodes when undergoes to a mechanical load. The amount of charge that a capacitor can store is defined as capacitance and depends by the geometrical property of the capacitor. So the **Capacitance** is 'stress-dependent' and can be used to generate sensing capabilities (For more details, refer to Section 3.2.1).

This thesis will therefore investigate the relationship between mechanical stresses and the electrical response of the piezoelectric material embedded in

⁹Figure was taken from the slides [8].

the composite through virtual manufacturing techniques.

2.3.1 Piezoelectrics Materials

In according to [8], this section presents the most commonly used piezoelectric materials in electromechanical experiments of this type. In particular, PZT (Lead Zirconate Titanate) of 4 different types: PZT-4, PZT-5H, PZT-5A and PZT-8. They are ceramics piezoelectrics materials with high piezoelectric constants and mechanical stiffness, widely used in sensors due to its high sensitivity. However, they are brittle and their minimum thickness can locally affect the mechanical properties of the structure.

Property	PZT-4	PZT-5H	PZT-5A	PZT-8	Unit
$\overline{E_1}$	81.3	60.3	60.6	93.63	GPa
E_2	81.3	60.3	60.6	93.63	GPa
E_3	64.5	47.8	53.2	74.23	GPa
$ u_{12}$	0.329	0.287	0.352	0.281	
$ u_{13}$	0.432	0.516	0.438	0.433	
ν_{23}	0.432	0.516	0.438	0.433	
G_{12}	25.6	23.5	22.5	29.32	GPa
G_{13}	25.6	23.0	21.0	29.32	GPa
G_{23}	30.6	23.0	21.0	29.32	GPa
e_{15}	12.72	17.04	12.26	7.08	C/m^2
e_{24}	12.72	17.04	12.26	7.08	C/m^2
e_{31}	-5.2	-6.55	-5.3	-0.557	C/m^2
e_{32}	-5.2	-6.55	-5.3	-0.557	C/m^2
e_{33}	15.88	22.97	15.8	8.659	C/m^2
χ_{11}	1.31e-8	1.50e-8	1.53e-8	1.14e-8	F/m
χ_{22}	1.31e-8	1.50e-8	1.53e-8	1.14e-8	F/m
χ_{33}	1.15e-8	1.33e-8	1.50e-8	8.85e-9	F/m

Table 2.1: Mechanical, piezoelectric, and dielectric properties of PZT-4, PZT-5H, PZT-5A, and PZT-8. ¹⁰

2.3.2 Temperature's effect

Temperature is described as a key factor in the curing processes of both thermosetting and thermoplastic resins. However, when dealing with composites that incorporate piezoelectric sensors, the curing temperature is limited by the Curie Temperature. If the temperature exceeds the Curie temperature, Tc, the permanent polarization of the piezoelectric material is lost. Nevertheless, the piezoelectric material may undergo depolarization even at temperatures below Tc, due to electrical or mechanical stresses.

Due to the impurities present in these materials or their different compositions, it is difficult to estimate precise Curie temperatures for each of them. In fact, the literature has noted that slightly different Curie temperature values exist from case to case. For the analyses conducted in this work, however, it will be important to work with sensors with the highest possible Curie temperature so that the temperature does not affect a key parameter used to calculate capacitance: **Absolute Permittivity** χ .

Absolute permittivity is easily calculated starting from the dielectric constant K with the following formula:

$$\varepsilon = K \cdot \varepsilon_0 = K \cdot 8.854 \cdot 10^{-12} F/m \tag{2.3}$$

After having found the trend of the dielectric constant as a function of temperature from the document [12], we then calculated the absolute permittivity as a function of temperature for the three materials: PZT-4, PZT-5H, and

¹⁰The mechanical and piezoelectric characteristics of PZT-4, PZT-5H and PZT-5A were obtained from paper [9]. The reported values of PZT-8 were estimated by applying the analytical expressions provided in Zhang et al. [10]. The dieletric properties of PZT-4, PZT-5H, PZT-5A and PZT-8 were estimated by [11]. Since the values are not directly reported by the authors, but rather extrapolated through independent calculation, their numerical accuracy cannot be fully quaranteed.

PZT-5A. The absolute permittivity values of PZT-8 were estimated by applying the analytical expressions provided in Zhang et al. [10].

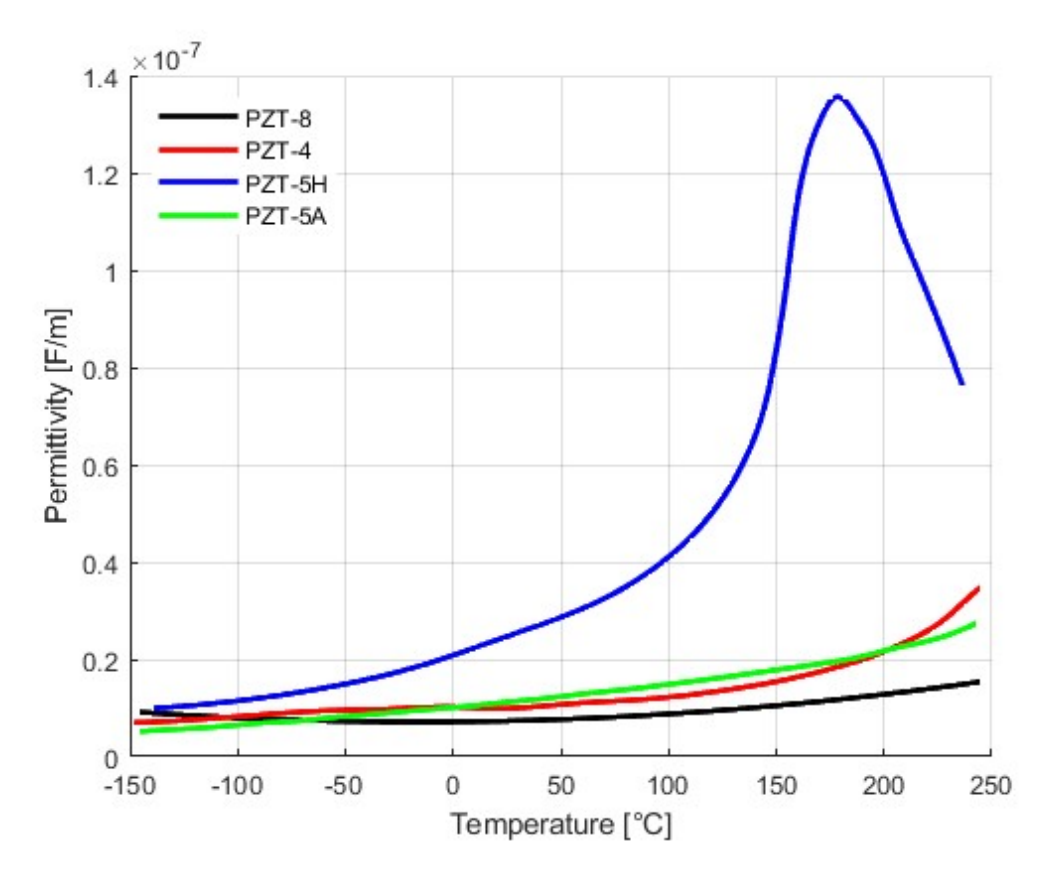


Figure 2.9: Permittivity of PZT-4, PZT-5H, PZT-5A and PZT-8

It is observed that the permittivity of PZT-5H explodes near 180°C, which is probably the Curie temperature of this type of piezoelectric material.

From a thermal perspective, the best piezoelectric material among the four considered is probably the PZT-8, which exhibits a fairly stable permittivity trend as the temperature increases.

The permittivity of the PZT-4 and PZT-5A exhibits a very similar trend as a function of temperature but it is not stable as the permittivity trend of PZT-8.

Chapter 3

Carrera Unified Formulation (CUF)

In this section is introduced the Carrera Unified Formulation (CUF) which was developed at Politecnico di Torino within the Department of Mechanical and Aerospace Engineering..

It is a multifunctional and robust technique used in structural engineering to analyze the behavior of complex structures, such as beams and plates.

With CUF, it is possible to model and solve structural problems of various kinds with high accuracy and it allows working with 3D, 2D, and 1D models. A fundamental feature of CUF is that it allows the derivation of the matrices and vectors involved in structural analysis into Fundamental Nuclei.

The **Fundamental Nuclei (FN)** are expressed in terms of four indexes : τ , s, i, and j. This FN is a 3 × 3 array (3 × 1 in the case of a vector) and its form does not change for 1D, 2D, or 3D problems. If the problem needs to an Electro-Mechanical Model the fundamental nucleus becomes 4x4. For this

thesis work, the focus will be on the study of the CUF applied to 1D models. It will be used **MUL2** code developed at POLITO and it will be described in the next chapter.

3.1 One-Dimensional Model¹

Classical 1D models are based on the dependence of their variables on a single coordinate (typically y), with x and z representing the coordinates of the cross-section. This is convenient for models with a compact cross-section, but it becomes less effective for models with a more complex geometry. Some methods for approximating the cross-section will be analyzed, which will determine their accuracy.

The displacement field of 1D models is described using the classical FE approach $N_i(y)$ along the axis and functions $u_i(x, z)$ over the cross-section:

$$u(x, y, z) = N_i(y)u_i(x, z)$$
(3.1)

Where:

- $N_i(y)$, used to approximate the displacements along the y-axis. The total number of elements is N_{BE} , each consisting of N_{NE} number of nodes.
- $u_i(x, z)$ is functions of the cross-section coordinates. It can be approximated by introducing a generic expansion for the cross-section. It can be written

¹Much of the content discussed in this section are taken from [13], especially from Chapters 8 and 9, which are dedicated to one-dimensional models employing Taylor and Lagrange expansions.

as the sum of the generic functions $F_{\tau}(x,z)$:

$$u_{i}(x,z) = F_{\tau}(x,z)u_{\tau i}$$

$$= F_{1}(x,z)u_{1i} + F_{2}(x,z)u_{2i} + \dots +$$

$$+ F_{\tau}(x,z)u_{\tau i} + \dots + F_{M}(x,z)u_{Mi}$$
(3.2)

where M is the number of terms in the expansion.

So the displacement field of 1D models (Fig 3.1) is described:

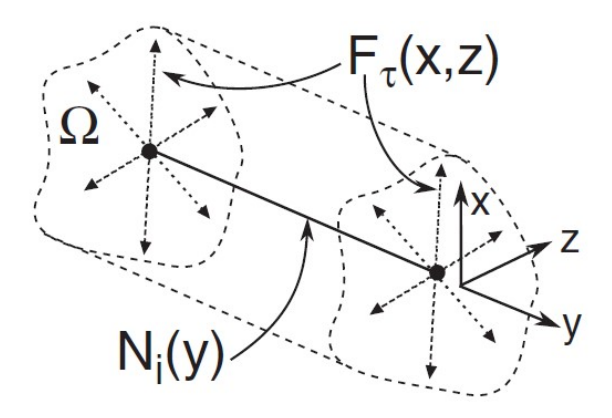


Figure 3.1: 1D Model $^{\rm 2}$

$$u(x, y, z) = N_i(y)F_{\tau}(x, z)u_{\tau i}$$
 (3.3)

 $F_{\tau}(x,z)$ can be obtained using both **Taylor Expansion** and **Lagrange Expansion**. Both will be analyzed, and then the fundamental nuclei of the stiffness matrix, obtained from the displacement fields, will be investigated.

²Figure was taken from [13].

3.1.1 Taylor Expansion (TE)

This section discusses classical models like Euler–Bernoulli beam Theory and Timoshenko beam Theory and introduces 1D elements based on Taylor-like expansions of displacement variables.

Classical Theory

The **Euler–Bernoulli beam Theory** (Fig.3.2), was derived from the following a priori assumptions:

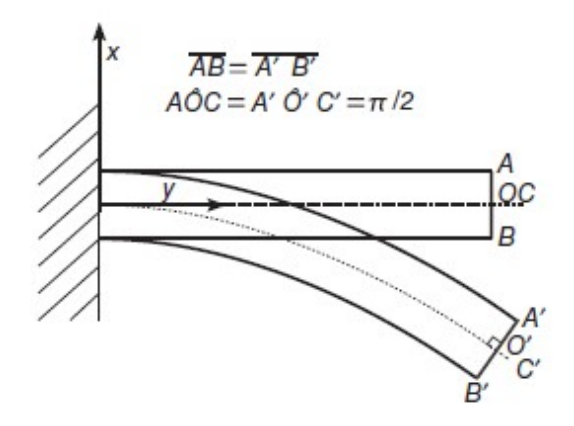


Figure 3.2: Euler-Bernoulli beam model 3

1. The cross-section is rigid on its plane.

$$\begin{cases}
\epsilon_{xx} = u_{x,x} = 0 \\
\epsilon_{zz} = u_{z,z} = 0 \\
\gamma_{xz} = u_{x,z} + u_{z,x} = 0
\end{cases}
\Rightarrow
\begin{cases}
u_x(x, y, z) = u_{x_1}(y) \\
u_z(x, y, z) = u_{z_1}(y)
\end{cases}$$
(3.4)

2. The cross-section rotates around a neutral surface, remaining plane.

$$u_y(x, y, z) = u_{y_1}(y) + \phi_z(y)x + \phi_x(y)z$$
(3.5)

³Figure was taken from [13].

where ϕ_z and ϕ_x are the rotation angles along the z- and the x-axis (negative direction), respectively.

3. The cross-section remains perpendicular to the neutral surface during deformation.

$$\begin{cases} \gamma_{xy} = u_{y,x} + u_{x,y} = \phi_z + u_{x_1,y} = 0 \\ \gamma_{yz} = u_{y,z} + u_{z,y} = \phi_x + u_{z_1,y} = 0 \end{cases} \Rightarrow \begin{cases} \phi_z = -u_{x_1,y} \\ \phi_x = -u_{z_1,y} \end{cases}$$
(3.6)

The displacement field is given by:

$$\begin{cases} u_x = u_{x_1} \\ u_y = u_{y_1} - u_{x_1, y} x - u_{z_1, y} z \\ u_z = u_{z_1} \end{cases}$$
 (3.7)

In **Timoshenko beam Theory** (Fig. 3.3), the cross-section is still rigid on its plane, it rotates around a neutral surface, remaining plane, but it is no longer constrained to remain perpendicular to it. So Shear deformations γ_{xy} and γ_{yz} are accounted for.

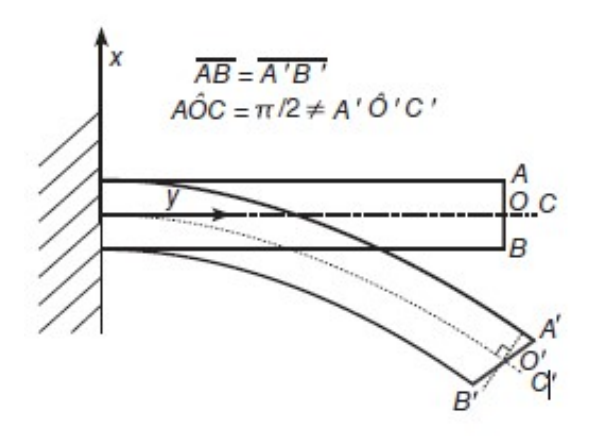


Figure 3.3: Timoshenko beam model ⁴

⁴Figure was taken from [13].

The displacement field of Timoshenko beam Theory is:

$$\begin{cases} u_x(x, y, z) = u_{x_1}(y) \\ u_y(x, y, z) = u_{y_1}(y) + \phi_z(y)x + \phi_x(y)z \\ u_z(x, y, z) = u_{z_1}(y) \end{cases}$$
(3.8)

Complete Linear Expansion Case

The complete linear expansion model includes a first-order (N = 1) Taylor-like polynomial to describe the cross-section displacement field

$$\begin{cases} u_x = u_{x_1} + xu_{x_2} + zu_{x_3} \\ u_y = u_{y_1} + xu_{y_2} + zu_{y_3} \\ u_z = u_{z_1} + xu_{z_2} + zu_{z_3} \end{cases}$$
(3.9)

- The first terms in 1: rigid translations (if the y-direction it is taken into account only, it would be a rod);
- The second terms in x: linear displacement in x/y/z with respect to x (contraction, bending and torsion);
- The third terms in z: linear displacement in x/y/z with respect to z

If a Taylor expansion have an order N greater than 1, the formulation can be written using the terms present in is in Table 3.1.

3.1.2 Lagrange Expansion (LE)

The Lagrange Expansion 1D models represent the second class of 1D models developed in the framework of the CUF. In an LE model, the F_{τ} expansion functions coincide with the Lagrange polynomials. The use of LE as F_{τ} does not

$\overline{\mathbf{N}}$	M	$\mathbf{F}_{ au}$
0	1	$F_1 = 1$
1	3	$F_2 = x, F_3 = z$
2	6	$F_4 = x^2, F_5 = xz, F_6 = z^2$
3	10	$F_7 = x^3$, $F_8 = x^2 z$, $F_9 = xz^2$, $F_{10} = z^3$
:	:	<u>:</u>
N	$\frac{(N+1)(N+2)}{2}$	$F_{\frac{N^2+N+2}{2}} = x^N, \dots, F_{\frac{(N+1)(N+2)}{2}} = z^N$

Table 3.1: Taylor-like polynomials

imply a reformulation of the problem equations and matrices, which is typical in the CUF environment.

In Fig. 3.4 are shown three type of Lagrange polynomials: L3, L4 and L9:

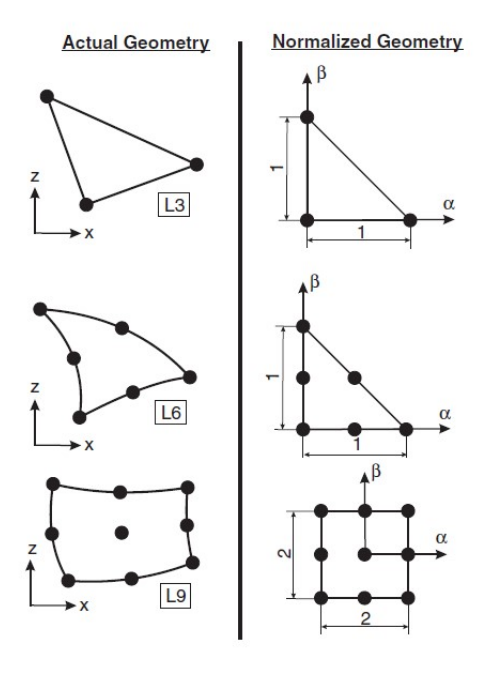


Figure 3.4: Lagrange Polynomials: L3, L4, L9 5

Lagrange polynomials are usually given in terms of normalized or natural

⁵Figure was taken from [13].

coordinates. This choice is not compulsory since LE polynomials can also be implemented in terms of actual coordinates. However, the normalized formulation was preferred since it offers many advantages.

Example: L9 Element

L9 polynomials and point coordinates are given by these Equations and Table 3.2:

$$\begin{cases}
F_{\tau} = \frac{1}{4}(\alpha^{2} + \alpha\alpha_{\tau})(\beta^{2} + \beta\beta_{\tau}), & \tau = 1, 3, 5, 7 \\
F_{\tau} = \frac{1}{2}\beta_{\tau}^{2}(\beta^{2} + \beta\beta_{\tau})(1 - \alpha^{2}) + \frac{1}{2}\alpha_{\tau}^{2}(\alpha^{2} + \alpha\alpha_{\tau})(1 - \beta^{2}), & \tau = 2, 4, 6, 8 \\
F_{\tau} = (1 - \alpha^{2})(1 - \beta^{2}), & \tau = 9
\end{cases}$$
(3.10)

Point	α_{τ}	β_{τ}
1	-1	-1
2	0	-1
3	1	-1
4	-1	0
5	0	0
6	1	0
7	-1	1
8	0	1
9	1	1

Table 3.2: Coordinates of the points with α_{τ} and β_{τ}

The L9 displacement field is given by

$$\begin{cases} u_x = F_1 u_{x1} + F_2 u_{x2} + F_3 u_{x3} + F_4 u_{x4} + F_5 u_{x5} + F_6 u_{x6} + F_7 u_{x7} + F_8 u_{x8} + F_9 u_{x9} \\ u_y = F_1 u_{y1} + F_2 u_{y2} + F_3 u_{y3} + F_4 u_{y4} + F_5 u_{y5} + F_6 u_{y6} + F_7 u_{y7} + F_8 u_{y8} + F_9 u_{y9} \\ u_z = F_1 u_{z1} + F_2 u_{z2} + F_3 u_{z3} + F_4 u_{z4} + F_5 u_{z5} + F_6 u_{z6} + F_7 u_{z7} + F_8 u_{z8} + F_9 u_{z9} \end{cases}$$

$$(3.11)$$

Cross-section Multi-elements and Locally Refined Models

Cross-sections can be discretized by means of multiple LE elements. This is a fundamental function of LE elements (this function will be explained in more detail in the assessment chapter). Multi-elements are generally adopted for three main purposes:

- 1. To refine the cross-section displacement field without increasing the polynomial expansion order.
- 2. To impose the geometrical discontinuities above the cross-section.
- 3. To refine the structural model locally.

3.1.3 Fundamental Nucleus

Starting from:

$$u(x, y, z) = N_i(y)F_{\tau}(x, z)u_{\tau i}$$
 (3.12)

it is possible to introduce the virtual variation using the s index instead of τ :

$$\delta u(x, y, z) = N_j(y)F_s(x, z)\delta u_{sj}$$
(3.13)

The shape functions N_i and N_j expand the solution from the nodes to the axis. Expansions F_{τ} and F_s expand the solution from the nodes to the cross-section of the bar (Fig.3.5).

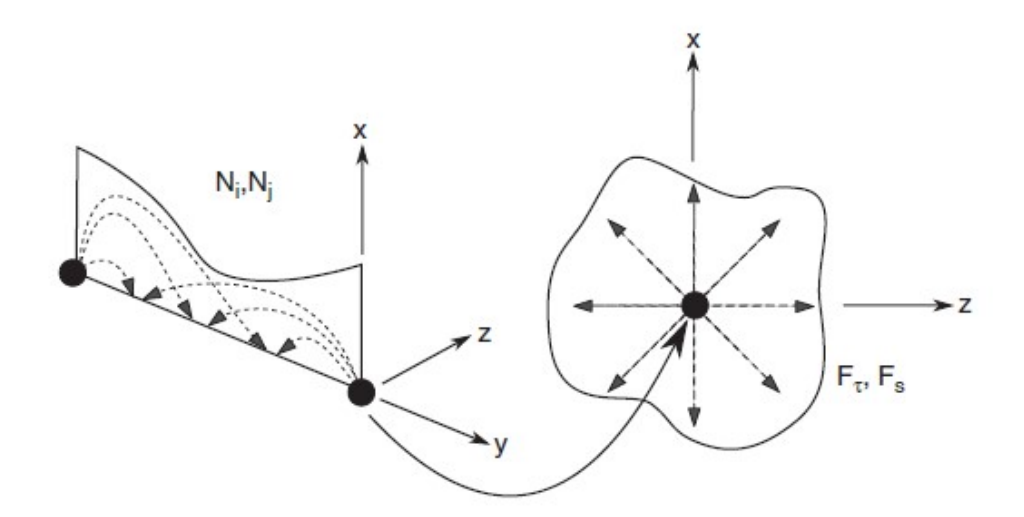


Figure 3.5: Axial approximation (N_i, N_j) , cross-section expansion (F_τ, F_s) 6

It is necessary to remember that Strains can be given in vectorial form,

$$\epsilon = bu \tag{3.14}$$

where b is a differential operator matrix of size 6×3 which contains the geometrical relation between the displacements and strains:

$$b = \begin{bmatrix} \frac{\partial}{\partial x} & 0 & 0\\ 0 & \frac{\partial}{\partial y} & 0\\ 0 & 0 & \frac{\partial}{\partial z}\\ \frac{\partial}{\partial z} & 0 & \frac{\partial}{\partial x}\\ 0 & \frac{\partial}{\partial z} & \frac{\partial}{\partial y}\\ \frac{\partial}{\partial y} & \frac{\partial}{\partial x} & 0 \end{bmatrix}$$
(3.15)

In this case, ε and σ are vectors that contain all the strain and stress

⁶Figure was taken from [13].

components:

$$\boldsymbol{\varepsilon} = \begin{pmatrix} \varepsilon_{xx} \\ \varepsilon_{yy} \\ \varepsilon_{zz} \\ \varepsilon_{xz} \\ \varepsilon_{yz} \\ \varepsilon_{yx} \end{pmatrix} \quad \text{and} \quad \boldsymbol{\sigma} = \begin{pmatrix} \sigma_{xx} \\ \sigma_{yy} \\ \sigma_{zz} \\ \sigma_{xz} \\ \sigma_{yz} \\ \sigma_{yz} \\ \sigma_{yx} \end{pmatrix}$$
(3.16)

The physical relationship between stress and strain components, in terms of stiffness coefficients, is

$$\sigma = C \epsilon \tag{3.17}$$

where C is a 6×6 matrix with all the material coefficients. It's provided an example of C for an isotropic material:

$$C = \begin{bmatrix} C_{11} & C_{12} & C_{12} & 0 & 0 & 0 \\ C_{21} & C_{11} & C_{12} & 0 & 0 & 0 \\ C_{21} & C_{21} & C_{11} & 0 & 0 & 0 \\ 0 & 0 & 0 & C_{44} & 0 & 0 \\ 0 & 0 & 0 & 0 & C_{44} & 0 \\ 0 & 0 & 0 & 0 & 0 & C_{44} \end{bmatrix}$$

$$(3.18)$$

So the strain, the virtual strain and the stress can be derived using the differential operator b and the material coefficient matrix C staring from

$$\delta u(x, y, z) = N_i(y) F_s(x, z) \delta u_{si}$$
(3.19)

to:

$$\epsilon(x, y, z) = bN_i(y)F_{\tau}(x, z)u_{\tau i}$$
(3.20)

$$\delta \epsilon(x, y, z) = bN_j(y)F_s(x, z)\delta u_{sj}$$
(3.21)

$$\sigma(x, y, z) = CbN_i(y)F_{\tau}(x, z)u_{\tau i}$$
(3.22)

The governing equations are derived by applying the Principle of Virtual Displacements (PVD). For a static problem:

$$\delta L_{\rm int} = \delta L_{\rm ext}$$
 (14)

where $L_{\rm int}$ represents the strain energy due to the deformation, and $L_{\rm ext}$ stands for the work done by the external loads on the virtual displacement. δ indicates the virtual variation. The internal work can be expressed as:

$$\delta L_{\text{int}} = \int_{V} \delta \epsilon^{T} \sigma \, dV$$

$$= \delta u_{sj}^{T} \int_{V} \left[F_{s}(x, z) N_{j}(y) b^{T} C b N_{i}(y) F_{\tau}(x, z) \right] dV u_{\tau i}$$
(3.23)

If all the components of the displacement are considered

$$b^T C b = [3 \times 6][6 \times 6][6 \times 3] = 3 \times 3$$

and the **Fundamental nucleus** becomes a 3×3 matrix :

$$k_{\tau sij} = \int_{V} F_s(x, z) N_j(y) b^T C b N_i(y) F_{\tau}(x, z) dV$$
(3.24)

This FN does not change for 1D, 2D, or 3D problems. The use of the CUF makes the assembly of the matrices a trivial operation that can be easily implemented in computer code. The assembly of the matrix consists of four loops on indices i, j, τ , and s, and an FN is calculated for each combination of these indices. The FN is the core, and the loops on τ and s build the matrix

for a given pair of i and j(Fig. 3.6 [a]). The loops on i and j give the matrix of the elements (Fig. 3.6 [b]), and the loop on the elements gives the global stiffness matrix (Fig. 3.6 [c]). It shows how it is possible to build a matrix of the node, of the element, and, finally, of the global stiffness matrix by exploiting the nucleus.

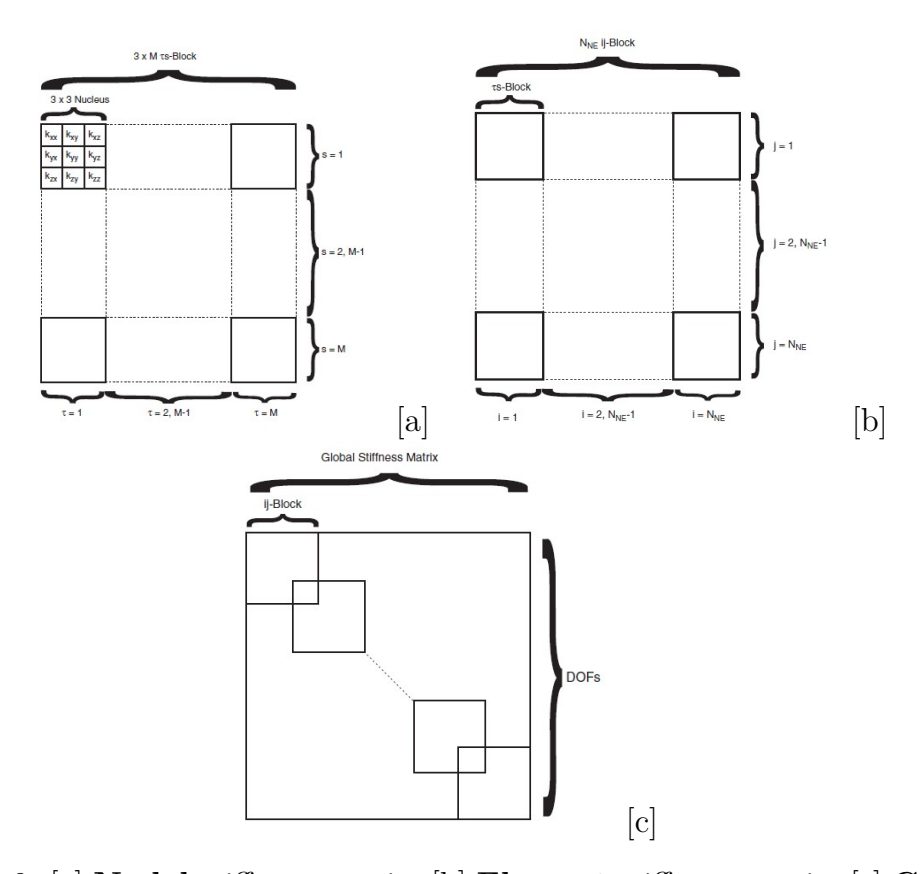


Figure 3.6: [a] **Nodal** stiffness matrix, [b] **Element** stiffness matrix, [c] **Global** stiffness matrix⁷

⁷Figure was taken from [13].

FE governing equations

Once the fundamental nuclei (3x3 matrices) are calculated and the global stiffness matrix is assembled, it is possible to derive the governing equations through the Principle of Virtual Displacements (PVD).

The internal work can be expressed as:

$$\delta L_{\text{int}} = \delta u_{sj}^T k_{\tau sij} u_{\tau i} \tag{3.25}$$

The loading vector in the case of a generic concentrated load P is

$$\mathbf{P} = \begin{cases} P_x \\ P_y \\ P_z \end{cases} \tag{3.26}$$

and the work due to \mathbf{P} is

$$\delta L^{\text{ext}} = \mathbf{P} \, \delta \mathbf{u}^T \tag{3.27}$$

Thus, the governing equation can be written as:

$$\delta L^{\text{ext}} = \delta L^{\text{int}} \tag{3.28}$$

$$\delta u_{si}^T k_{\tau sij} u_{\tau i} = \mathbf{P} \, \delta \mathbf{u}^T \tag{3.29}$$

DOFs and Comparing TE with LE

The **Total number of DOFs** of the structural model will be given by:

$$DOFs = (3 \times M) \times [(N_{NE} - 1) \times N_{BE} + 1]$$
 (3.30)

where:

- $(3 \times M)$: number of DOFs per node.
 - M depends on the choice made to approximate the F_{τ} :
 - If **TE** (Tensor Expansion) has been chosen:
 - * It depends on the order up to which the polynomial has been expanded.
 - If **LE** (Lagrange Elements) has been chosen:
 - * It depends on which element has been used on the section (L3, L4, L9, ...).
 - * It also depends on how many subsections the section has been divided into.
- N_{NE} : number of nodes per element (along the length);
- N_{BE} : total number of beam elements along the length (y-axis).

3.2 Electro-Mechanical Model⁸

Considering the electric potential ϕ as a primary variable in a coupled piezoelectric model, a generalised 4×1 displacement vector \mathbf{q} can be adopted:

$$\mathbf{q} = \begin{bmatrix} u_x \\ u_y \\ u_z \\ \phi \end{bmatrix} \tag{3.31}$$

The 3×1 electric field vector **E** can be derived as:

$$\mathbf{E} = \begin{bmatrix} E_x \\ E_y \\ E_z \end{bmatrix} = \begin{bmatrix} \frac{\partial}{\partial x} \\ \frac{\partial}{\partial y} \\ \frac{\partial}{\partial z} \end{bmatrix} \phi \tag{3.32}$$

The generalized 9×1 strain vector $\bar{\boldsymbol{\varepsilon}}$ can be written as:

strain vector
$$\tilde{\boldsymbol{\varepsilon}}$$
 can be written as:
$$\begin{bmatrix} \varepsilon_{xx} \\ \varepsilon_{yy} \\ \varepsilon_{zz} \\ \varepsilon_{xz} \\ \varepsilon_{yz} \\ \varepsilon_{xy} \\ E_x \\ E_y \\ E_z \end{bmatrix}$$
(3.33)

where the general matrix of the differential operator $\bar{\mathbf{D}}$ is a 9 × 4 matrix given by:

⁸Much of the content discussed in this section are taken from [9]

$$\bar{\mathbf{D}} = \begin{bmatrix}
\frac{\partial}{\partial x} & 0 & 0 & 0 \\
0 & \frac{\partial}{\partial y} & 0 & 0 \\
0 & 0 & \frac{\partial}{\partial z} & 0 \\
\frac{\partial}{\partial z} & 0 & \frac{\partial}{\partial x} & 0 \\
0 & \frac{\partial}{\partial z} & \frac{\partial}{\partial y} & 0 \\
\frac{\partial}{\partial y} & \frac{\partial}{\partial x} & 0 & 0 \\
0 & 0 & 0 & -\frac{\partial}{\partial x} \\
0 & 0 & 0 & -\frac{\partial}{\partial z} \\
0 & 0 & 0 & -\frac{\partial}{\partial z}
\end{bmatrix}$$
(3.34)

In the case of the principle of virtual displacement (PVD), the electromechanical constitutive equations (stress-charge form or e-form) can be expressed by:

$$\boldsymbol{\sigma} = \mathbf{C}\boldsymbol{\varepsilon} - \mathbf{e}^T \mathbf{E}$$

$$\mathbf{D}_e = \mathbf{e}\boldsymbol{\varepsilon} + \boldsymbol{\chi}^S \mathbf{E}$$
(3.35)

where \mathbf{D}_e is the 3×1 electric displacement vector

$$\mathbf{D}_e = \begin{bmatrix} D_x \\ D_y \\ D_z \end{bmatrix}, \quad \boldsymbol{\sigma} \text{ is the } 6 \times 1 \text{ mechanical stress vector,}$$

 ${\bf C}$ is the 6 × 6 stiffness matrix of mechanical material coefficients, and ${\boldsymbol \varepsilon}$ is the 6 × 1 strain vector. The superscripts E and S indicate evaluation at constant electric field and strain, respectively.

The 3×3 dielectric permittivity matrix evaluated at constant stress, $\boldsymbol{\chi}^{S}$, is given by:

$$\boldsymbol{\chi}^{S} = \begin{bmatrix} \chi_{11}^{S} & \chi_{12}^{S} & 0\\ \chi_{21}^{S} & \chi_{22}^{S} & 0\\ 0 & 0 & \chi_{33}^{S} \end{bmatrix}$$
(3.36)

The piezoelectric stiffness coefficient matrix e is a 3×6 matrix given by:

$$\mathbf{e} = \begin{bmatrix} e_{11} & e_{12} & e_{13} & e_{14} & e_{15} & e_{16} \\ e_{21} & e_{22} & e_{23} & e_{24} & e_{25} & e_{26} \\ e_{31} & e_{32} & e_{33} & e_{34} & e_{35} & e_{36} \end{bmatrix}$$
(3.37)

The generalized stress vector can be definited as:

$$\begin{cases}
\sigma_{xx} \\
\sigma_{yy} \\
\sigma_{zz} \\
\sigma_{xz}
\end{cases} =
\begin{bmatrix}
C_{11}^{E} & C_{12}^{E} & C_{13}^{E} & 0 & 0 & C_{16}^{E} & -e_{11} & -e_{21} & -e_{31} \\
C_{21}^{E} & C_{22}^{E} & C_{23}^{E} & 0 & 0 & C_{26}^{E} & -e_{12} & -e_{22} & -e_{32} \\
C_{31}^{E} & C_{32}^{E} & C_{33}^{E} & 0 & 0 & C_{36}^{E} & -e_{13} & -e_{23} & -e_{33} \\
\sigma_{xz} \\
\sigma_{yz} \\
\sigma_{xy}
\end{cases} =
\begin{bmatrix}
C_{11}^{E} & C_{12}^{E} & C_{23}^{E} & 0 & 0 & C_{26}^{E} & -e_{12} & -e_{22} & -e_{32} \\
C_{31}^{E} & C_{32}^{E} & C_{33}^{E} & 0 & 0 & C_{36}^{E} & -e_{13} & -e_{23} & -e_{33} \\
0 & 0 & 0 & C_{44}^{E} & C_{45}^{E} & 0 & -e_{14} & -e_{24} & -e_{34} \\
\varepsilon_{xz} \\
\varepsilon_{xz} \\
\varepsilon_{xz} \\
\varepsilon_{yz}
\end{cases} =
\begin{bmatrix}
C_{11}^{E} & C_{12}^{E} & C_{13}^{E} & 0 & 0 & C_{36}^{E} & -e_{13} & -e_{23} & -e_{33} \\
0 & 0 & 0 & C_{44}^{E} & C_{45}^{E} & 0 & -e_{14} & -e_{24} & -e_{34} \\
\varepsilon_{xz} \\
\varepsilon_{xz} \\
\varepsilon_{yz}
\end{cases} =
\begin{bmatrix}
C_{11}^{E} & C_{12}^{E} & C_{13}^{E} & 0 & 0 & C_{13}^{E} & -e_{13} & -e_{23} & -e_{33} \\
0 & 0 & 0 & C_{44}^{E} & C_{55}^{E} & 0 & -e_{15} & -e_{25} & -e_{35} \\
\varepsilon_{yz} \\
\varepsilon_{xy}
\end{cases} =
\begin{bmatrix}
C_{11}^{E} & C_{12}^{E} & C_{13}^{E} & 0 & 0 & C_{14}^{E} & -e_{14} & -e_{24} & -e_{34} \\
\varepsilon_{xz} \\
\varepsilon_{yz}
\end{cases} =
\begin{bmatrix}
C_{11}^{E} & C_{12}^{E} & C_{13}^{E} & 0 & 0 & C_{14}^{E} & -e_{13} & -e_{23} & -e_{33} \\
\varepsilon_{xz}
\end{cases} =
\begin{bmatrix}
C_{11}^{E} & C_{12}^{E} & C_{13}^{E} & 0 & 0 & C_{14}^{E} & -e_{14} & -e_{24} & -e_{34} \\
\varepsilon_{xz}
\end{cases} =
\begin{bmatrix}
C_{11}^{E} & C_{12}^{E} & C_{13}^{E} & 0 & 0 & C_{14}^{E} & -e_{13} & -e_{23} & -e_{33} \\
\varepsilon_{xz}
\end{cases} =
\begin{bmatrix}
C_{11}^{E} & C_{12}^{E} & C_{13}^{E} & 0 & 0 & C_{14}^{E} & -e_{13} & -e_{23} & -e_{33} \\
\varepsilon_{xz}
\end{cases} =
\begin{bmatrix}
C_{11}^{E} & C_{12}^{E} & C_{13}^{E} & 0 & 0 & C_{14}^{E} & -e_{13} & -e_{24} & -e_{34} \\
\varepsilon_{xz}
\end{cases} =
\begin{bmatrix}
C_{11}^{E} & C_{12}^{E} & C_{13}^{E} & 0 & 0 & C_{14}^{E} & -e_{13} & -e_{24} & -e_{34} \\
\varepsilon_{xz}
\end{cases} =
\begin{bmatrix}
C_{11}^{E} & C_{12}^{E} & C_{13}^{E} & 0 & 0 & C_{14}^{E} & -e_{13} & -e_{24} & -e_{25} \\
\varepsilon_{xz}
\end{cases} =
\begin{bmatrix}
C_{11}^{E} & C_{12}^{E} & C_{13}^{E} & 0 & 0 & C_{14}^{E} & -e_{13} & -e_{24} & -e_{25} \\
\varepsilon_{xz}
\end{cases} =
\begin{bmatrix}
C_{11}^{E} & C_{12}^{E} & C_{13}^{E} & 0 & 0 & C_{14}^{E} & -e_{13}^{E} & -e_{13} & -e_{24} \\
\varepsilon$$

(3.38)

and in compact form as:

$$\bar{\sigma} = \tilde{\mathbf{H}} \,\bar{\varepsilon} \tag{3.39}$$

where $\tilde{\mathbf{H}}$ is a generalized material property matrix that couples the mechanical and electrical fields.

If the piezoelectric components are poled in the third material axis, the dielectric permittivity matrix χ^S simplifies to:

$$\boldsymbol{\chi}^{S} = \begin{bmatrix} \chi_{11}^{S} & 0 & 0 \\ 0 & \chi_{22}^{S} & 0 \\ 0 & 0 & \chi_{33}^{S} \end{bmatrix}$$
 (3.40)

and the piezoelectric stiffness coefficient matrix \mathbf{e} reduces to the following form:

$$\mathbf{e} = \begin{bmatrix} 0 & 0 & 0 & e_{15} & 0 & 0 \\ 0 & 0 & 0 & 0 & e_{24} & 0 \\ e_{31} & e_{32} & e_{33} & 0 & 0 & 0 \end{bmatrix}$$
(3.41)

The displacement field of 1D models in the mechanical case was described as:

$$u(x, y, z) = N_i(y) F_{\tau}(x, z) u_{\tau i}$$
(3.42)

Extending this equation into the electromechanical case one can obtain:

$$q(x, y, z) = N_i(y)F_{\tau}(x, z)q_{\tau i}(y)$$
(3.43)

3.2.1 Capacitance Variation

The electromechanical constitutive equations given by Equation 3.35 could be manipolated ([9]) and it can be obtain:

$$\varepsilon = \mathbf{s}^{E} \, \sigma + \mathbf{d}^{T} \mathbf{E}$$

$$\mathbf{D}_{e} = \mathbf{d} \, \sigma + \boldsymbol{\chi}^{t} \, \mathbf{E}$$

$$37$$
(3.44)

where:

- σ , ε are the 6×1 stress and strain vectors
- $\mathbf{s}^E = (\mathbf{C}^E)^{-1}$ is the 6×6 compliance matrix (at constant electric field)
- $\mathbf{d} = \mathbf{e} \left(\mathbf{C}^E \right)^{-1}$ is the 3×6 electromechanical coupling matrix
- $\chi^t = \mathbf{e} \left(\mathbf{C}^E \right)^{-1} \mathbf{e}^T + \chi^S$ is the 3×3 permittivity matrix at constant stress
- **E** is the 3×1 electric field vector
- \mathbf{D}_e is the 3×1 electric displacement vector

It is important to emphasize that the coupling coefficient "d" (or "e" in the previous notation) remains nonzero as long as the Curie temperature is not exceeded. Once this temperature is surpassed, the piezoelectric effect is lost.

In a simplified case where $d_{15} = d_{24} = 0$, and where:

- The piezoelectric material is poled along the 3-direction
- The 1–2 plane is coated with electrodes (normal to the 3-axis)
- The electric field is applied only in the thickness (3) direction
- The material has symmetry about the 3-axis

The expanded form of the piezoelectric constitutive equations under the given assumptions becomes:

$$\begin{cases}
\varepsilon_{1} \\
\varepsilon_{2} \\
\varepsilon_{3} \\
\varepsilon_{4}
\end{cases} =
\begin{bmatrix}
s_{11}^{E} & s_{12}^{E} & s_{13}^{E} & 0 & 0 & 0 & d_{31} \\
s_{12}^{E} & s_{11}^{E} & s_{13}^{E} & 0 & 0 & 0 & d_{31} \\
s_{13}^{E} & s_{13}^{E} & s_{33}^{E} & 0 & 0 & 0 & d_{33} \\
\varepsilon_{4} \\
\varepsilon_{5} \\
\varepsilon_{6} \\
D_{3}
\end{bmatrix}
\begin{cases}
\sigma_{1} \\
\sigma_{2} \\
\sigma_{3} \\
\sigma_{3} \\
\sigma_{4}
\end{cases}$$

$$(3.45)$$

where:

- s_{ij}^E are the elements of the mechanical compliance matrix (at constant electric field),
- d_{ij} are the electromechanical coupling coefficients,
- D_3 and E_3 are the electric displacement and electric field components in the 3-direction,
- χ^t_{33} is the permittivity at constant mechanical stress in the 3-direction.

In the Cartesian coordinate system, the blocked (or embedded) capacitance is described as:

$$C = \frac{Q}{V} = \frac{H_A \oint_A D_z \, dx \, dy}{V} \tag{3.46}$$

where:

- Q is the total free charge,
- \bullet V is the applied potential difference,
- D_z is the electric displacement in the thickness (3) direction,

• H_A is a constant depending on electrode configuration or integration area (optional).

substituting the value of the electrical displacement from Equation (3.45) in Equation 5.8, we get:

$$C = \frac{\int \int_A (d_{31}\sigma_1 + d_{31}\sigma_2 + d_{33}\sigma_3) + \left(\chi_{33}^t \cdot \frac{V}{t}\right) dx dy}{V}$$
(3.47)

where t is the thickness of the piezoelectric layer,

In this expression:

- The first part of the integrand, involving $\sigma_1, \sigma_2, \sigma_3$, represents the *capacitance variation due to mechanical loading*.
- The second term in the integrand, $\chi_{33}^t \cdot \frac{V}{t}$, corresponds to the *free capacitance* of a parallel plate piezoelectric capacitor.

Chapter 4

Assessment

In the following chapter, After a brief description of the numerical model MUL 2 developed at Polito, several assessments will be analyzed to verify the effectiveness and characteristics of the numerical code MUL 2 Polito. This chapter will allow for the comparison of the different models proposed by this code for FEM simulation and provide insight into its advantages and limitations.

In the **First assessment**, a comparison will be made between the analytical and numerical calculations of the displacement w of a doubly clamped beam loaded at mid-span. Furthermore, the displacement w will be obtained considering both the Lagrange-Expansion model and the Taylor-Expansion model.

In the **Second assessment**, the problem of an eight-layered cantilever composite beam from paper [14] will be replicated. This problem involves a multilayer beam loaded at the free end, considering both the LE and TE models, and comparing the results. In this case, not only will the displacements w be compared, but also some stresses at specific points.

In the **Third assessment**, a multi-physics problem from paper [1] will be

reproduced. In this case, a piezoelectric patch will be used as an actuator, bonded to a clamped aluminum beam, in order to replicate the results presented in the paper and to correctly model the problem. Subsequently, the beam will be loaded at its free end, and the piezoelectric patch will act as a sensor. The results will be obtained in terms of voltage V and electric field E_z , using both Q9 and Q4 elements to observe the differences between the two formulations.

4.1 MUL 2 Polito

MUL2 is a software developed by the MUL2 research group at Politecnico di Torino.

Figure 4.1: Codice MUL 2

The software is composed of several input files that, before each analysis, will be modified according to the characteristics of the proposed problems. Afterwards, once the code is *launched* through the command prompt, it will be possible to view the results from the output files using either a text editor or a graphical program (such as Paraview).

The input files are illustrated below:

• NODES: contains the geometric coordinates of the nodes used in the structural model, defined in the global reference system, and defines the

type of implemented expansion (TE: Taylor Expansion, LE: Lagrange Expansion, etc.), and, if necessary, the corresponding expansion order;

- **CONNECTIVITY**: defines the type and number of finite elements used to construct the model;
- BC: allows the definition of boundary conditions related to a point or a plane (constraints or loads);
- EXP_CONN: contains the type of element used to describe the cross-section;
- EXP_MESH_NN: allows the definition of the geometric coordinates of the nodes in a certain local reference system of the cross-section;
- **VERSORS**: defines the unit vectors used to characterize the directions of the axes of the local reference system;
- MATERIAL: describes the material used and its related properties. It is possible to use isotropic and orthotropic materials;
- LAMINATION: allows the definition of the characteristics of the various material layers;
- ANALYSIS: allows the selection of the type of analysis to be performed (101: static analysis);
- POSTPROCESSING: returns the requested outputs.

The software will first be used for static analyses of very simple structures in the two proposed assessments. Later, it will be modified to allow multi-field static analyses (with integrated piezoelectric sensors), in which displacement fields and electric fields interact.

4.2 Assessment 1

In the first assessment, a simple problem of a doubly clamped beam subjected to a central load will be simulated. The displacement of the beam will be evaluated both analytically and numerically. The analytical solution will be derived using classical beam theory, while the numerical analysis will be performed using the MUL 2 FEM code through static analysis. Once both results are obtained, they will be compared in order to assess the accuracy and reliability of the numerical model. The material of the beam shown above is isotropic, and in this case,

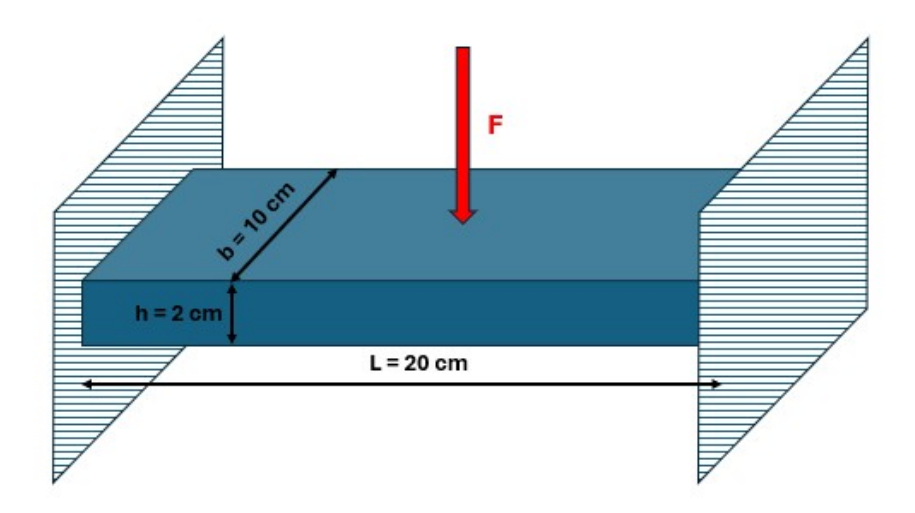


Figure 4.2: Modello Assessment 1

aluminum is chosen and its properties are shown in Tab.4.1.

It is loaded at its midpoint on the upper part by a force $F = -1000 \,\mathrm{N}$ and is doubly supported at the ends.

As the first step, the maximum displacement is calculated analytically (non trovo la fonte attendibile ma solo un sito online). Since the load is applied at the midpoint, the maximum displacement will also occur at the midpoint. Considering the section of the beam, the moment of inertia is calculated first,

Properties of Aluminum	Value
Young's Modulus (E)	$73000\mathrm{MPa}$
Poisson's Ratio (ν)	0.3
Density (ρ)	$2700.0\mathrm{kg/m}^3$

Table 4.1: Properties of Aluminum

followed by the maximum deflection that can be derived using the (4.2), derived from beam theory:

$$I = \frac{bh^3}{12} = \frac{(100mm)(20mm^3)}{12} = 66666.66mm^4 \tag{4.1}$$

$$\delta_{max} = \frac{FL^3}{192EI} = \frac{(-1000N)(200mm)^3}{192(73000N/mm^2)(66666.66mm^4)} = 8.56\mu m \tag{4.2}$$

Once the analytical solution is calculated, the same solution will be computed numerically using the Mul 2 code to perform a comparison and verify its accuracy.

4.2.1 Modeling

Several results were obtained by performing a static analysis using both Taylor Expansion models and Lagrange Expansion models along the **Length** and along the **Width** of the beam, by carefully examining the displacements of the points placed at the center of the beam along its length and along its width and interpolating the corresponding results of u_z .

In the case of the Lagrange Expansion models, numerical simulations were then carried out using sections with 1, 2, or 3 sub-sections, where the original section was divided vertically. This three section of LE models are shown in the following and every subsection uses an element L9 well described in 3.1.2:

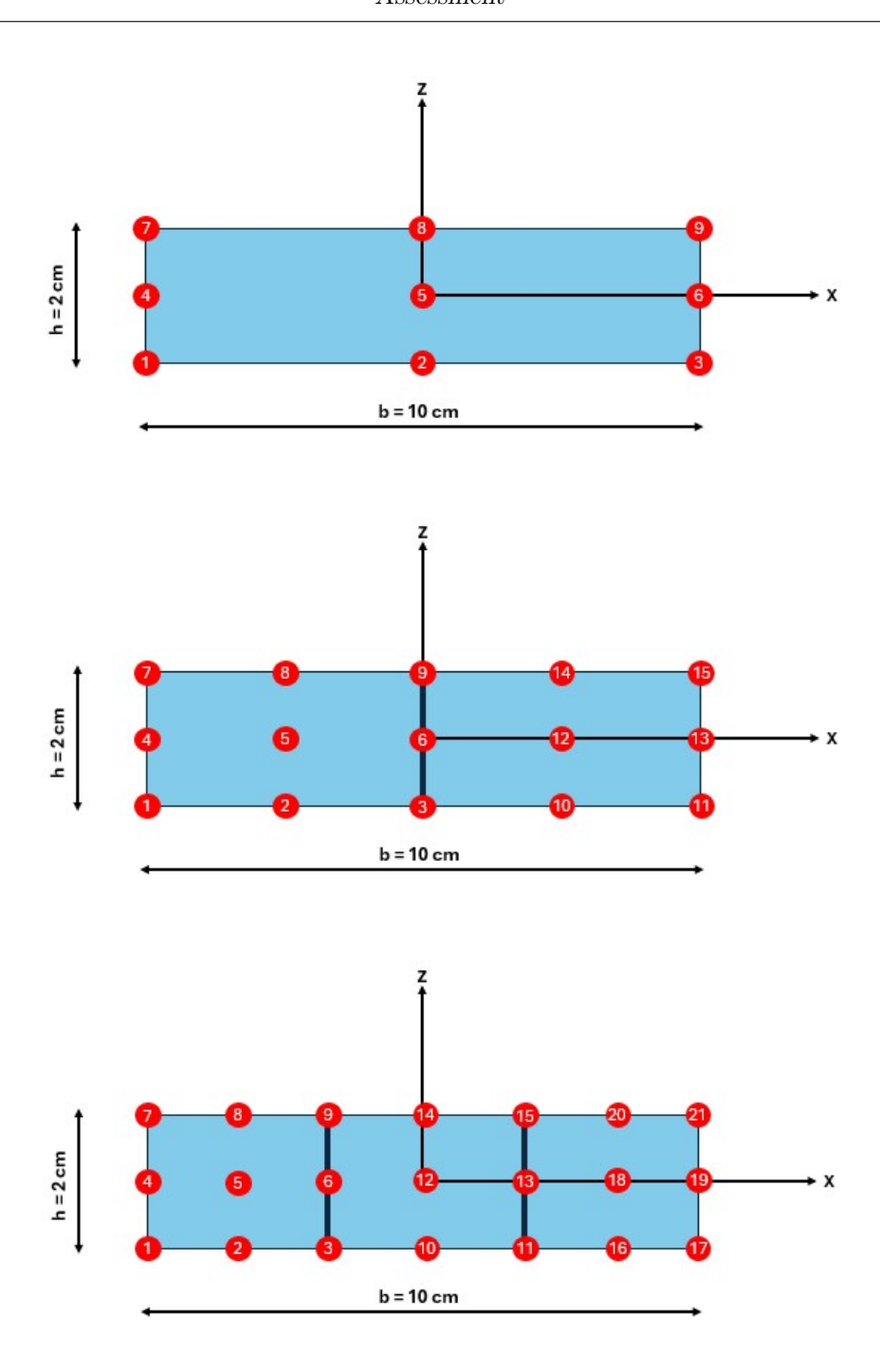


Figure 4.3: LE with 1,2 or 3 Subsections (With L9 elements)

4.2.2 Displacement u_z along the Length of the Beam

In this section, the difference in displacements u_z at certain points along the length of the beam will be observed, and some considerations will be made. It has been decided to take as reference the vertical section located at the center of the beam. The u_z displacements at different points of this section, located at z = 0, x = 0, and variable y, will be plotted and interpolated.

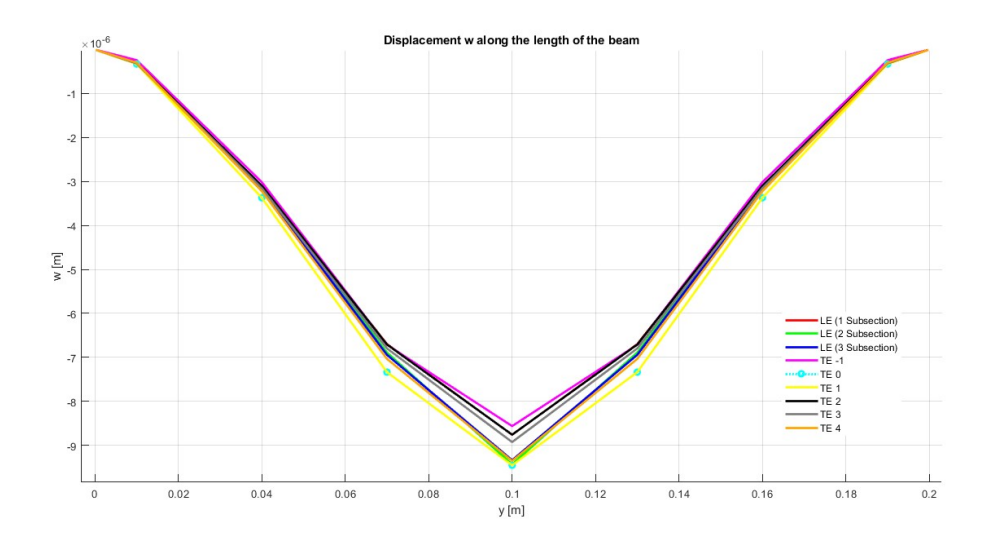


Figure 4.4: Displacement w [µm]

The main differences observed are around the midpoint of the beam, where the maximum displacement occurs.

Therefore, the following is provided a zoom of the differences in the displacement at the midpoint in Fig.4.8. The numerical results of the maximum displacement for each type of model are provided in Tab.4.2

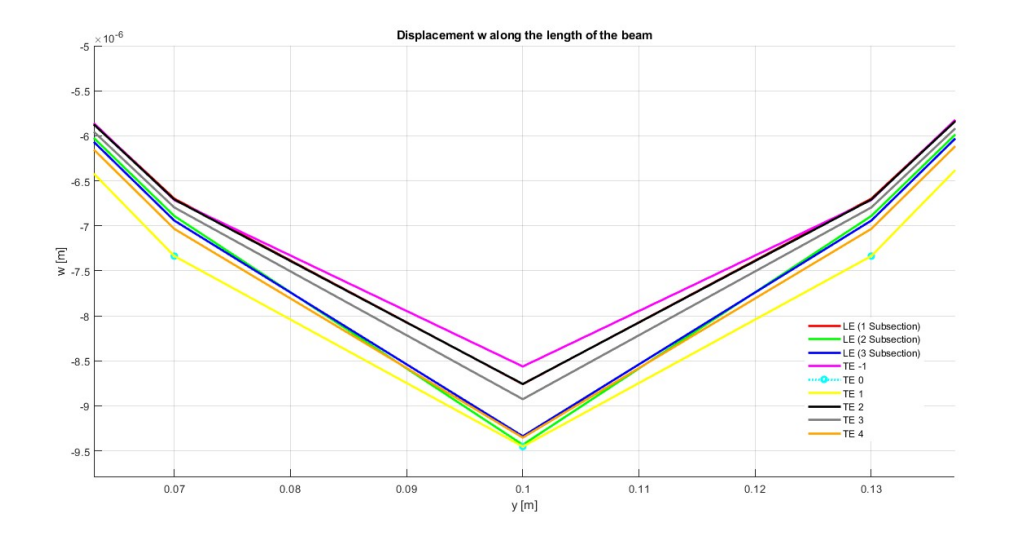


Figure 4.5: Zoom of Displacement w [µm]

Model	Maximum Deflection $[\mu m]$	DOFs
Analytical Solution	-8.561	_
TE -1	-8.562	279
TE 0	-9.452	279
TE 1	-9.452	279
TE 2	-8.757	558
TE 3	-8.926	930
TE 4	-9.353	1395
LE (1 Subsection)	-8.759	837
LE (2 Subsection)	-9.432	1395
LE (3 Subsection)	-9.338	1953

Table 4.2: Maximum Deflection for each type of model

Several observations can be made:

• The result of TE -1, which corresponds to the Euler-Bernoulli beam theory, is identical to the result obtained analytically from the beam theory previously.

• The result of TE 0 is equal to TE 1 because, in TE 0, which corresponds to Timoshenko theory, it is approximated as in formula (4.3), while in TE 1, it is approximated as in formula (4.4). Since it is a 1D model, this does not lead to any substantial difference.

$$\begin{cases} u_x = u_{x1}(y) \\ u_y = u_{y1}(y) + xu_{y2} + zu_{y3} \\ u_z = u_{z1}(y) \end{cases}$$
(4.3)

$$\begin{cases} u_x = u_{x1} + xu_{x2} + zu_{x3} \\ u_y = u_{y1} + xu_{y2} + zu_{y3} \\ u_z = u_{z1} + xu_{z2} + zu_{z3} \end{cases}$$

$$(4.4)$$

 Additionally, it is noted that as the order of TE increases, it converges towards the same result obtained with LE with 3 subsections, the most precise of the three LEs since it is the one in which more DOFs have been used.

In Fig.4.6 and in Fig.4.7 the displacement is shown along the beam both for the case with TE of order 4 and for the case with LE with 3 subsections. It can be observed that there is a substantial difference in how the displacements are displayed due to the different models used.

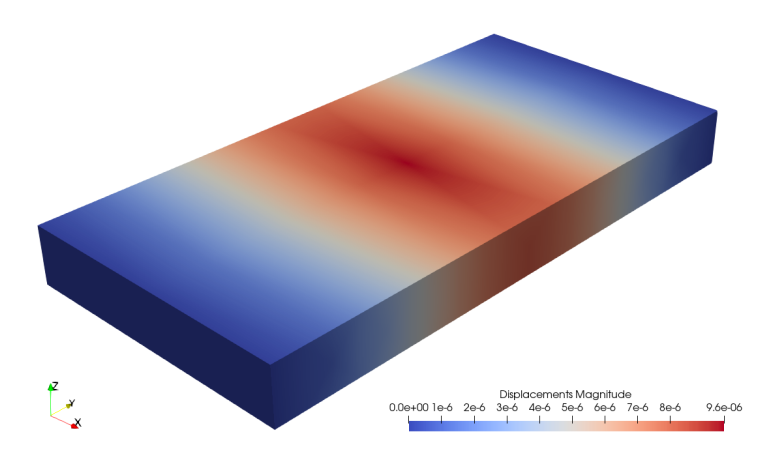


Figure 4.6: Displacement (TE 4)

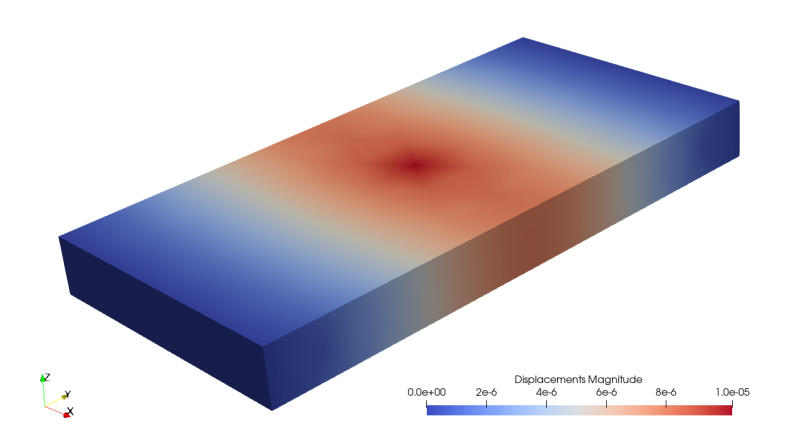


Figure 4.7: Displacement (LE with 3 Subsections)

4.2.3 Displacement u_z along the Width of the Beam

In the same way as done in the previous section, the trend of displacements u_z along the median line of a section can be observed. It has been decided to take as reference the vertical section located at the center of the beam, which will experience the largest displacements. The u_z displacements at different points of this section, located at z = 0, y = L/2, and variable x, will be plotted and interpolated.

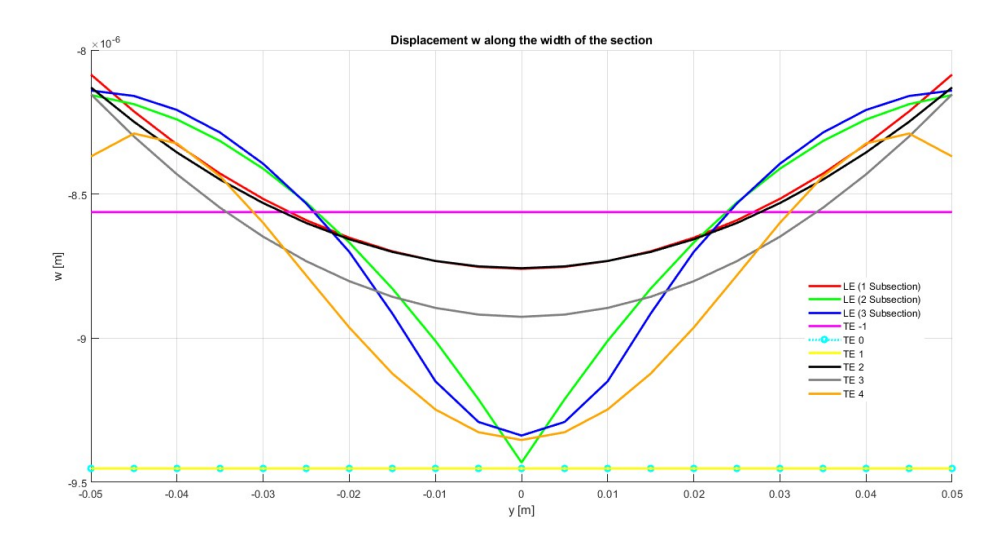


Figure 4.8: Displacement w along the width[m]

4.2.4 Considerations

It is therefore possible to observe from the Fig. 4.8 substantial differences between the different models used to model the beam. Many more differences are observed compared to what was previously observed in the section on the displacements u_z along the length of the beam.

Several observations can be made:

- First of all, TE-1, TE 0, and TE 1 are all linear displacement models, unable to capture how the section actually deforms, but rather give an overall idea of the deformation. In this case as well, TE 1 obviously coincides with Timoshenko, and TE 0 = TE 1, since the model considered is one-dimensional (1D) as seen previously.
- LE 1 coincides with TE 2, thus demonstrating that the two are equivalent under these modeling assumptions.

It can be observed that TE 2 uses the following 6 terms in the approximation:

$$1$$

$$x+z$$

$$x^2+2xz+z^2$$

LE 1, on the other hand has the result that is very similar to that of TE 2. But it uses the following 9 terms:

$$1$$

$$x + z$$

$$x^{2} + 2xz + z^{2}$$

$$3x^{2}z + 3xz^{2}$$

$$6x^{2}z^{2}$$

- LE 2 and LE 3 converge towards the correct solution due to their high number of nodes. LE 3 is more accurate than LE 2, at the cost of a significantly higher number of nodes (LE 3: 1953 DOFs, LE 2: 1395 DOFs).
- It can also be observed that increasing the order of the Taylor expansion (from TE 2 to TE 3) increases the central displacement of the section. However, only with TE 4 does the result become very close to that of LE 3.
- With TE 4, an anomalous behavior is noticed at the ends of the section when compared to the more accurate behavior observed with LE 3. It is therefore hypothesized that a fourth-order Taylor expansion can accurately approximate the displacement at the center, but not at the ends of the section.

4.3 Assessment 2

In the second assessment, the problem of a multilayer beam is reproduced from the paper [14]. The goal will be to reproduce the same results presented in the paper in order to understand how the Mul2 Polito code works. Some further considerations will then be discussed.

The beam will be fixed at one end and loaded at the free end with a force of 0.2 N at the center, as shown in the figure: The beam consists of 8 layers,

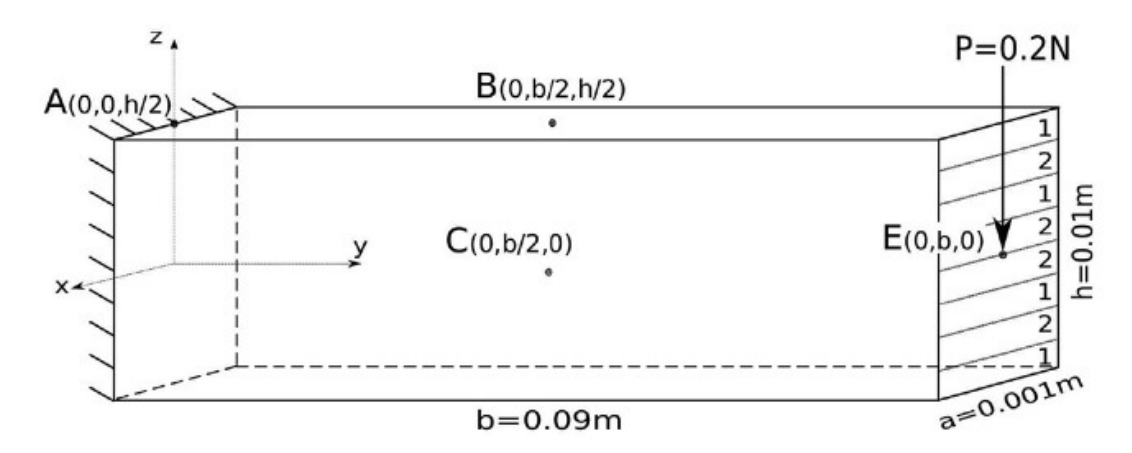


Figure 4.9: Model Assessment 2 1

and the materials used are 2 orthotropic materials with the properties listed in Tab.4.3.

	E_L [GPa]	E_T [GPa]	ν_{LT}	G_{LT}
Mat-1	30	1	0.25	0.5
Mat-2	5	1	0.25	0.5

Table 4.3: Properties of the Materials

¹Figure was taken from [14].

4.3.1 Modeling

In Fig.4.10 is shown the material composition of each layer of the multilayer beam.

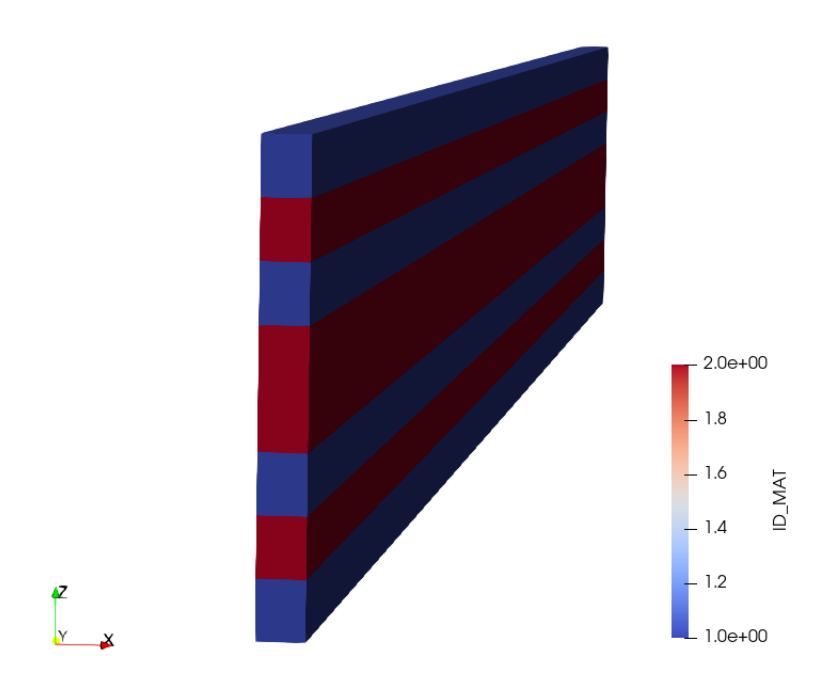


Figure 4.10: Materials (Blue=1, Red=2)

To compare the results with the paper, it is decided to evaluate the results at points A, B, C, and D, the coordinates of which are shown in Tab.4.4.

Point	Coordinates
A	[0,0,h/2]
В	[0, b/2, h/2]
\mathbf{C}	[0, b/2, 0]
D	[0, b, 0]

Table 4.4: Points A,B,C and D

The numerical results of each model in each Point are reported in Tab.4.5. It can be observed that the results are almost identical to those presented in paper [14]. The results obtained using the Lagrange expansion method, as reported in the paper, are also included in the table to allow for a better comparison.

Model	A: σ_{yy} [MPa]	B: $\sigma_{yy} \times 10^3$ [MPa]	C: $\sigma_{yz} \times 10^2$ [MPa]	D: $w \times 10^{-2}$ [mm]	DOFs
LE	1.708	730.168	-2.792	-3.054	4743
LE - Paper [14]	1.689	729.600	-2.794	-3.049	4743
TE 2	1.461	730.139	-2.006	-2.991	588
TE 3	1.610	730.169	-2.821	-3.035	930
TE 4	1.610	730.156	-2.821	-3.039	1395
TE 5	1.691	730.173	-2.750	-3.040	1953

Table 4.5: Stress evaluation at Points A, B, C, displacement w at point D and DOFs

4.3.2 Analysis through the thickness of a multilayer beam

For an analysis through the thickness of a multilayer beam is considered the section at the free estremities of the beam (Fig. 4.11).

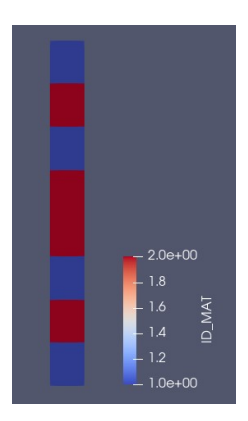


Figure 4.11: Section across z-axis

The displacement w along the z-axis is shown in Fig. 4.12. It can be observed that the displacement w obtained using the LE model is piecewise continuous, while the displacement w obtained with the TE models is continuous. As the

order of the Taylor expansion increases, the approximation of the displacement w improves. It is noticeable that with a third-order expansion, the result becomes quite close to the expected behavior, although it does not fully capture the detailed behavior, especially in the central laminae where the displacement w is more significant. On the contrary, the displacements u and v exhibit a linear trend across all the models considered (Fig. 4.13 and Fig. ??).

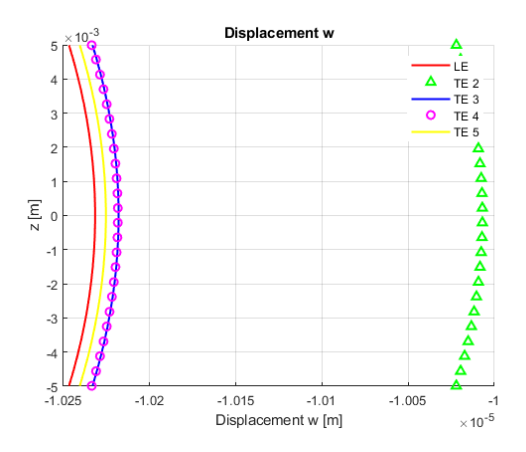


Figure 4.12: Displacement w

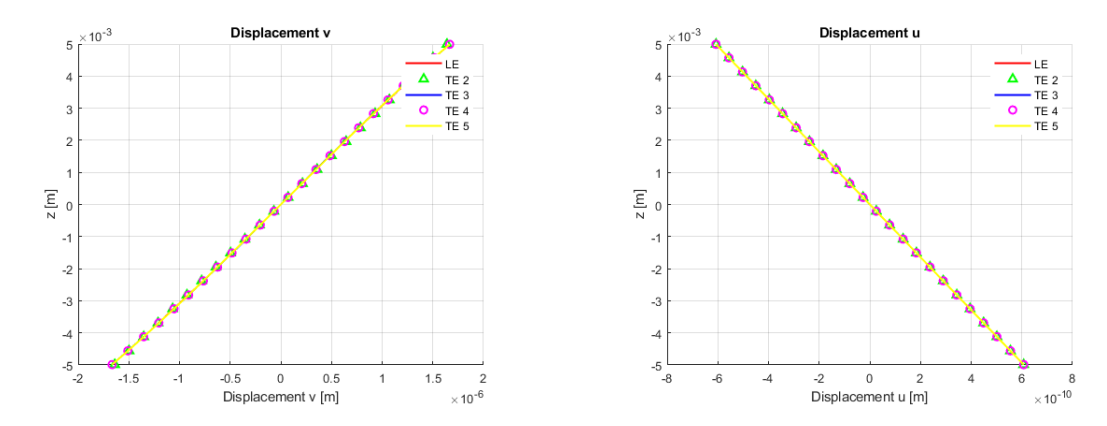


Figure 4.13: Displacements \mathbf{v} and \mathbf{u}

The deformations ϵ_{yy} , ϵ_{zz} , ϵ_{yz} and the stress σ_{yy} , σ_{zz} , σ_{yz} are therefore shown according to the respective models used:

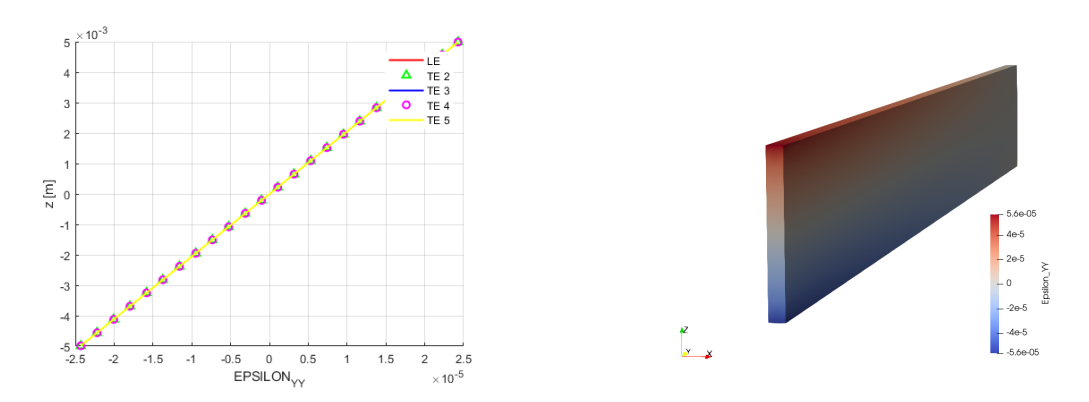


Figure 4.14: Strain ε_{yy} , TE5

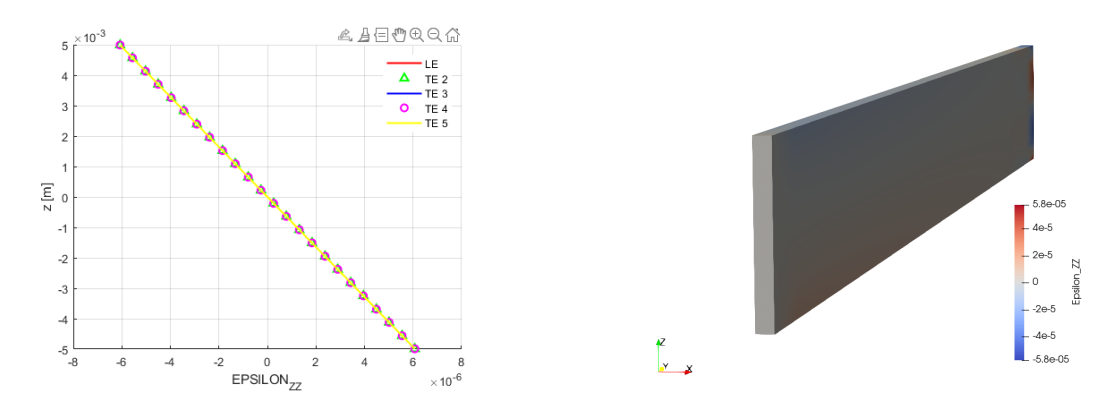


Figure 4.15: Strain ε_{zz} , TE5

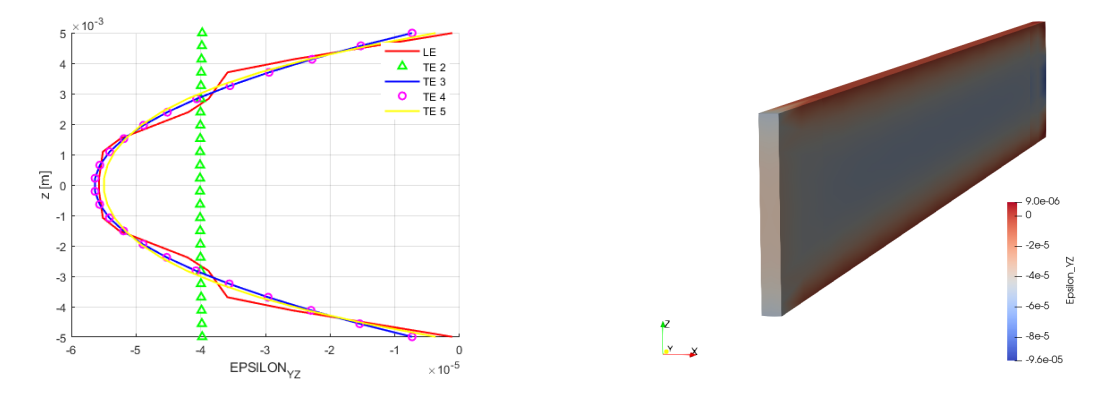


Figure 4.16: Strain ε_{yz} , TE5

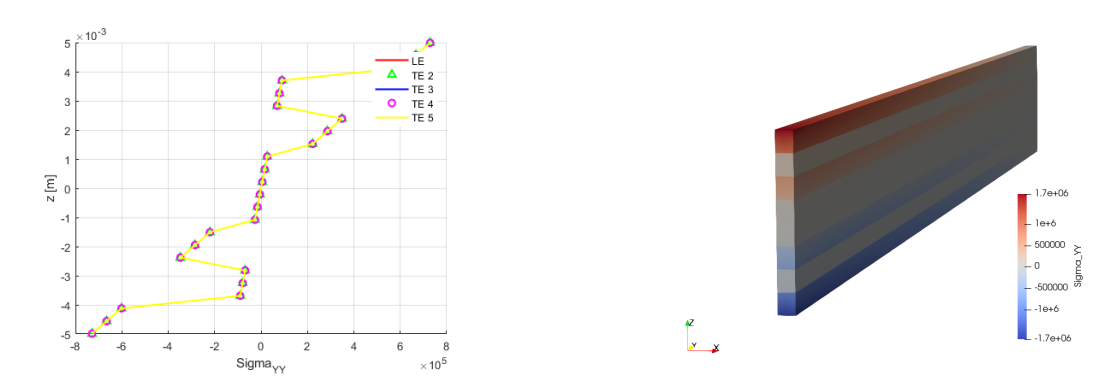


Figure 4.17: Stress σ_{yy} , TE5

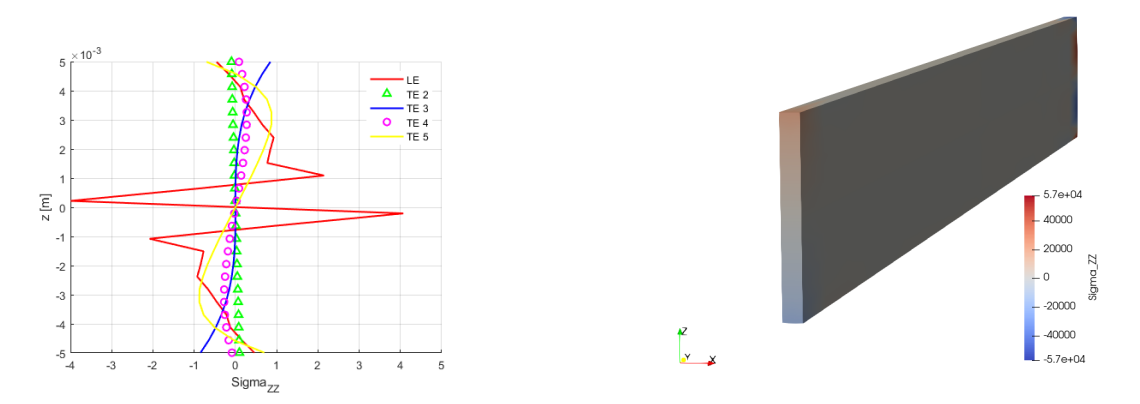


Figure 4.18: Stress σ_{zz} , TE5

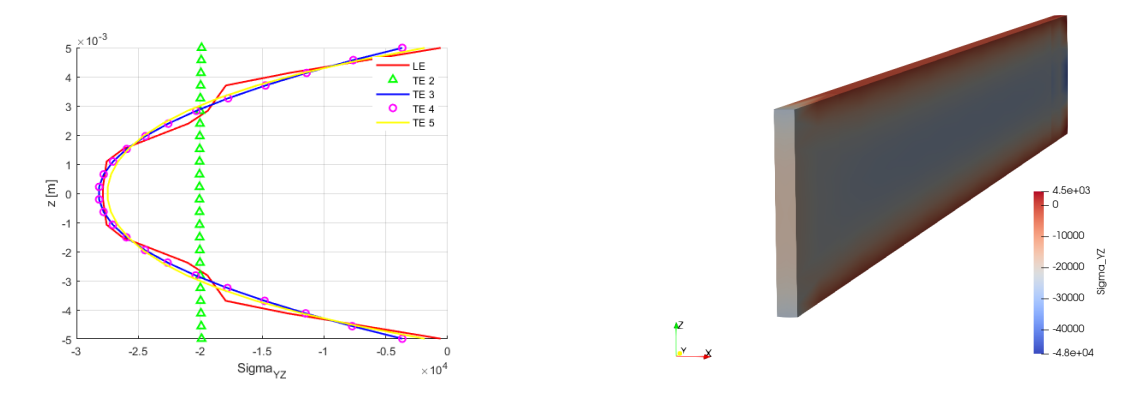


Figure 4.19: Stress σ_{yz} , TE5

4.3.3 Considerations

It can be observed that the TE model approximates the entire section more uniformly compared to the LE model. On the other hand, the LE model allows for a more precise representation of the deformations and stresses.

The linear behavior of the normal strains ε_{yy} and ε_{zz} , combined with the parabolic shape of the shear strain ε_{yz} , confirms that the beam undergoes classical bending with shear deformation effects. This is consistent with higher-order theories, where transverse shear strains are not neglected.

The piecewise continuity of the stress components σ_{yy} , σ_{zz} , and σ_{yz} reflects the presence of material interfaces in the multilayered beam. Although the stresses are continuous within each individual layer, they exhibit jumps in slope at the interfaces due to differences in mechanical properties between materials 1 and 2.

Overall, the mechanical response is consistent with the expected behavior of a composite laminated beam subjected to bending.

4.4 Assessment 3

In the third assessment, a multi-physics problem is introduced. The problem, studied in paper [1], is illustrated in Figure 4.20. It involves a clamped aluminum beam, to which a patch of piezoelectric material PZT-4 is applied near the clamped upper end.

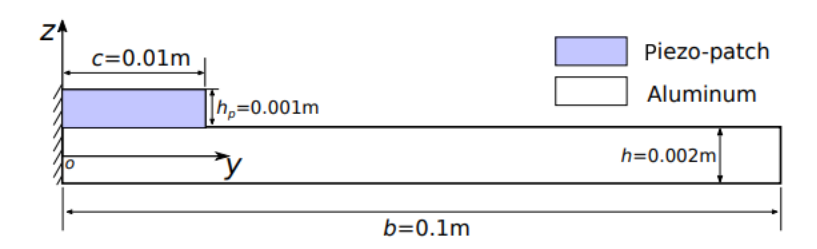


Figure 4.20: Side View



Figure 4.21: Top View

The properties of the piezoelectric material are listed in Tab.2.1.

Initially, the piezoelectric patch will act as an actuator. To this end, an electric potential of 1V is applied to its top surface and 0V to the bottom. Once the results are compared with those reported in the paper and the model is verified to be correctly implemented, the patch will be used as a sensor instead of an actuator.

In this second configuration, the aluminum beam will be loaded at its free end with an external force, and the resulting variation in voltage V and electric field Ez within the patch will be measured. Finally, a comparison will be made between the results obtained using Q9 and Q4 elements in the section.

4.4.1 Actuator

A finer mesh of B4 elements was chosen (as in paper [1]) in the region of the piezoelectric patch and in the area immediately adjacent to it, up to 2 cm from the clamped end. The remaining 8 cm of the beam were modeled with a lower density of B4 elements. For the cross-section, Q9 elements were used—one for the aluminum beam section and one for the piezoelectric patch section.

In this assessment case, the piezo-patch acts as an actuator, and an electrical potential of 1V is defined on its top surface and 0V on the bottom. This configuration is shown in Figure 4.22:

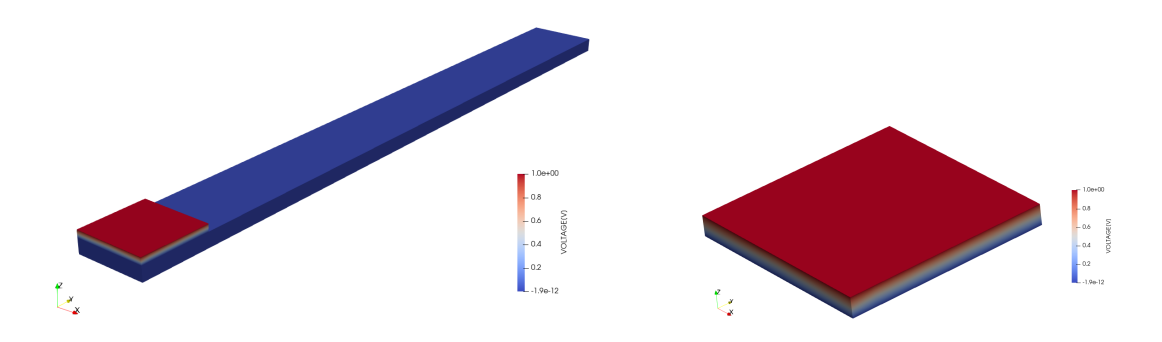


Figure 4.22: Voltage [V]

The potential difference applied to the piezoelectric patch generates an electric field.

This causes the patch to deform, and consequently, since the patch is bonded

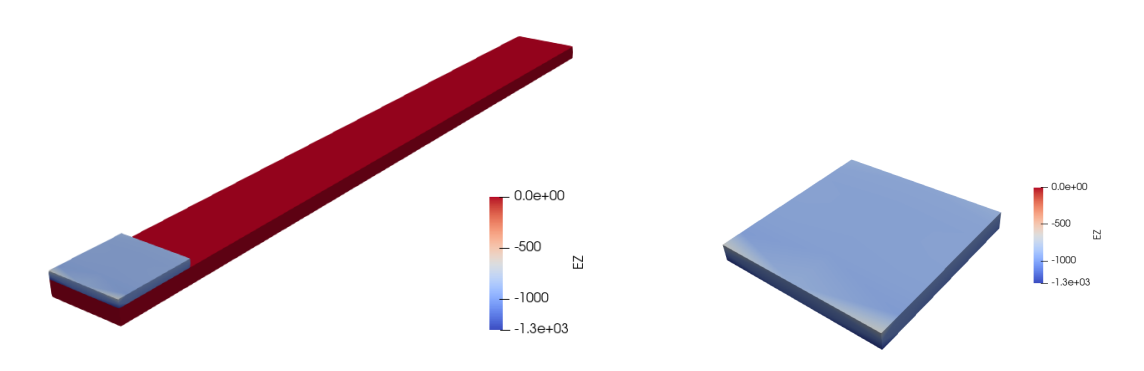


Figure 4.23: E_z

to the beam, the beam will deform as well (Fig. 4.24).

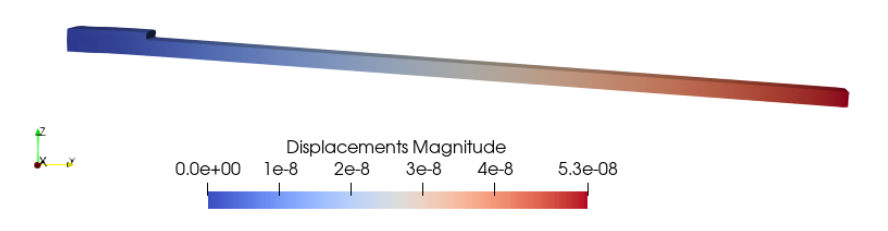


Figure 4.24: Displacement w[m]

Tab. 4.6 shows a comparison between the results obtained in this work and those reported in Paper [1]. The small differences observed can be attributed to the use of a mesh with approximately 1000 fewer degrees of freedom (DOFs), resulting in a significantly simplified model. The model used in Paper [1] employs 2LE9 elements in both the piezoelectric and mechanical cross-sections, with each consisting of 2×1 ($x \times z$) sub-domains.

Figure 4.25 also show the trends of the displacement w and the stress component σ_{yy} along the y-axis of the beam. It can be observed that they follow

Mesh	DOFs	$-u_z[10^{-8}m]$	$-u_z[10^{-8}m]$	$-\sigma_{yy}[KPa]$	$-\sigma_{yz}[KPa]$
		(0, b/2, 0)	(0, b, 0)	(0, c/2, -h/2)	(a/2, c/2, 0)
Paper	2250	2.482	5.192	5.878	0.5149
Results	1350	2.5	5.2	4.8	0.45

Table 4.6: Comparison with Results from the Paper [1]

the same trend as the results reported in [1].

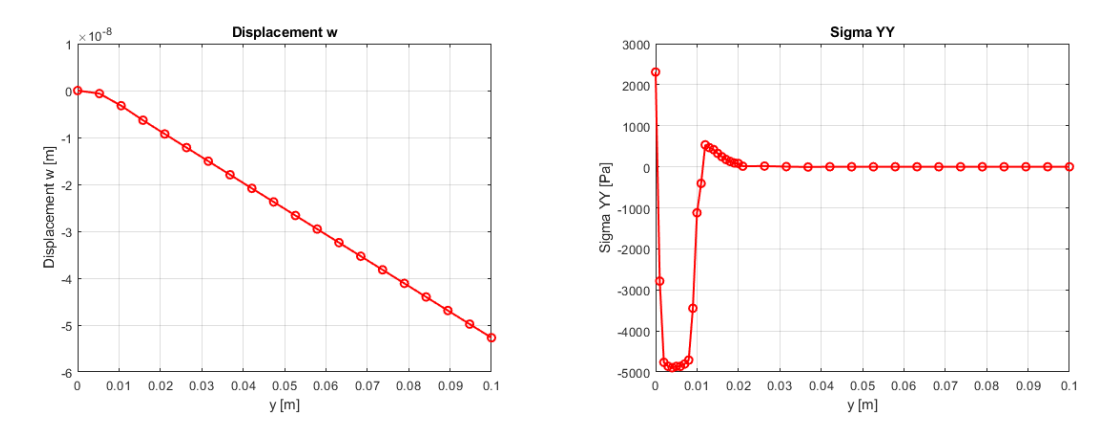


Figure 4.25: Displacement w(0,y,0) and σ_{yy} (0,y,-h/2)

4.4.2 Sensor - Model with elements Q9

In the sensor case, the exact same mesh as in the actuator case was used.

In this case, however, the aluminum beam was modeled as a piezoelectric material with high electrical conductivity, so that it effectively acts as an electrode on the bottom surface of the piezoelectric patch. Moreover, the electric potential on the top surface of the piezoelectric patch was set to zero, ensuring a constant voltage across the thickness and thus simulating the presence of an electrode on the top surface as well.

As a first step, a force of 20N is applied at the center of the free end, and the resulting displacements are observed in Fig. 4.26

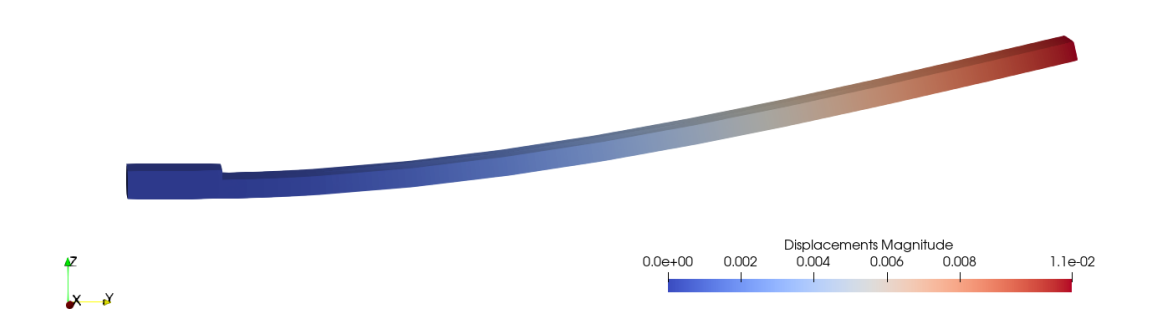


Figure 4.26: Displacement w

Due to the piezoelectric effect, a mechanical stress along the y-axis generates an electric field along the z-axis (i.e., through the thickness of the patch) via the piezoelectric coefficient d_{32} . The direction of the resulting electric field depends on whether the material is under tension or compression, as well as on the polarization direction of the piezoelectric material.

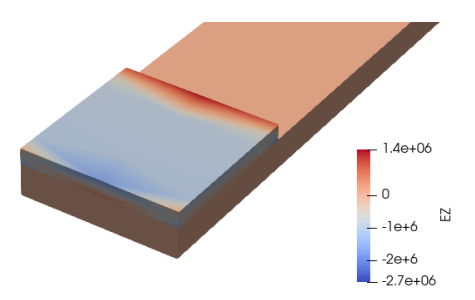


Figure 4.27: E_z

The electric field E_z , when integrated across the patch thickness, generates a potential difference (Fig. 4.28) between the two electrodes (the top and bottom surfaces of the patch):

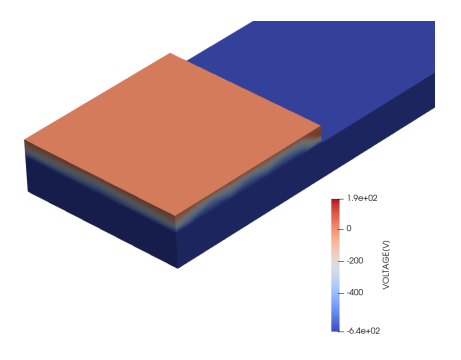


Figure 4.28: Voltage V

By considering only the piezoelectric patch (Fig. 4.29), it is possible to analyze the relationship between the electric field and the resulting voltage.

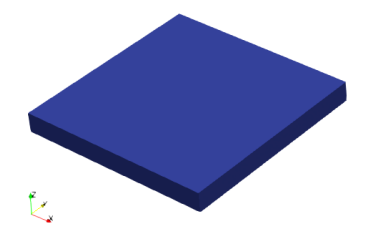


Figure 4.29: Patch Piezoelettrica

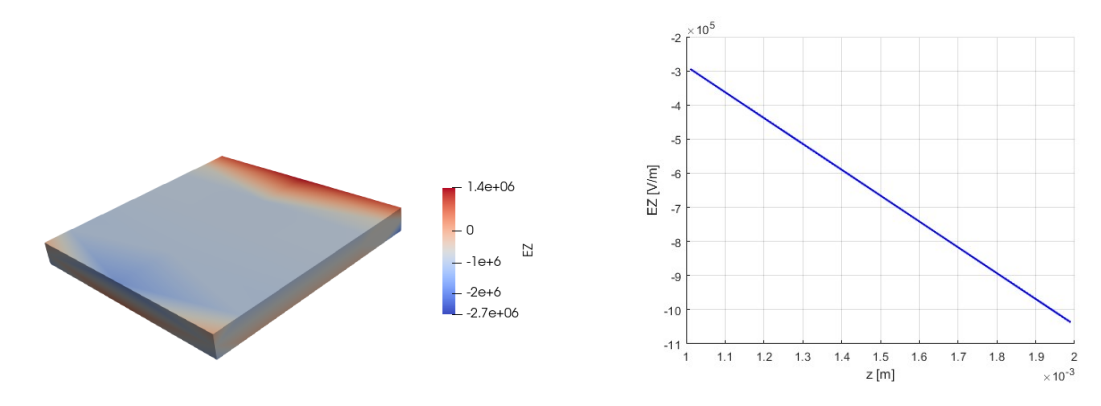


Figure 4.30: E_z

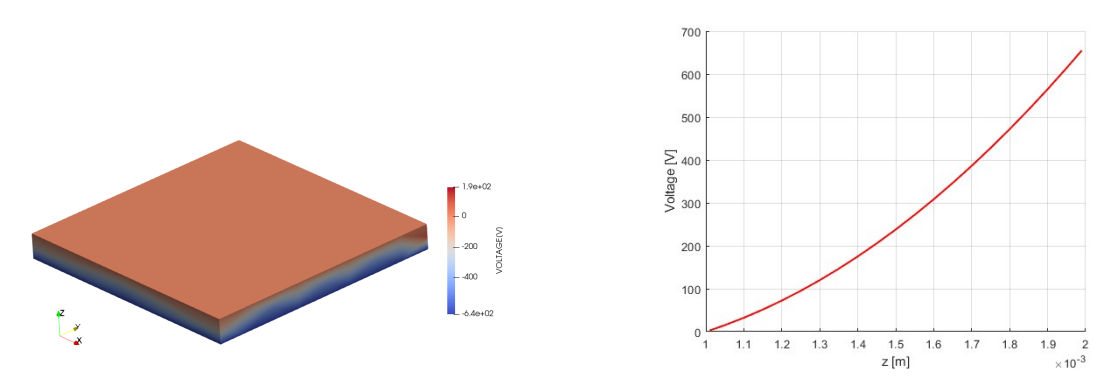


Figure 4.31: Voltage V

For the graphs shown above, the central axis of the piezoelectric patch along the thickness direction (along z) was taken as the reference point. Indeed, it can be observed that the behavior is not uniform across the entire width of the plate, making the choice of the reference point for the measurements of E_z and voltage crucial.

In Fig. 4.30, it can be observed how the Q9 elements on the section allow us to visualize a linear electric field that decreases from 0.001 mm (contact point between the piezoelectric patch) to 0.002 mm (thickness of the piezoelectric patch).

Considering a one-dimensional electric field along the thickness direction of

the piezoelectric patch (the z-axis), the following relation holds:

$$E(z) = -\frac{dV}{dz}$$

If the electric field E(z) varies linearly along the thickness, it can be expressed as:

$$E(z) = az + b$$

where a and b are constants determined by boundary conditions. Integrating this expression, we obtain the Voltage V(z):

$$V(z) = -\int E(z) dz = -\int (az + b) dz = -\frac{a}{2}z^2 - bz + C$$

It follows that, if the electric field is linear through the thickness, the electric potential assumes a quadratic profile, as can indeed be observed in Fig. 4.31.

Sensor - Model with elements Q4

The same problem was modeled using Q4 elements along the cross-section (Fig. 5.7), instead of the previously used Q9 elements. This was done in order to observe the differences between linear elements (Q4) and quadratic elements (Q9), and to assess whether both types of elements are capable of accurately representing a quadratic field such as the electric potential V. In this case,

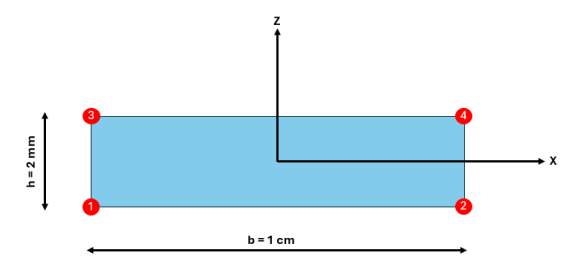


Figure 4.32: Q4 Element

the force was still applied at the free end of the beam, but not at the center of the cross-section, as Q4 elements do not allow for this positioning directly. As a result, the displacement (Fig. 4.33) differs from the previous case (with element Q9), which is expected. However, this discrepancy is not of interest in the present analysis, as the objective is solely to compare the qualitative behavior of the electric field E_z and the electric potential V when using Q4 elements.

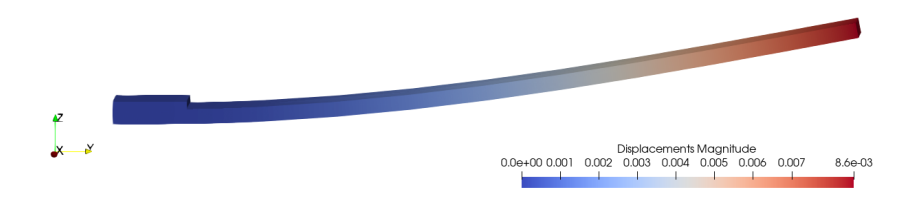


Figure 4.33: Displacement w (with element Q4)

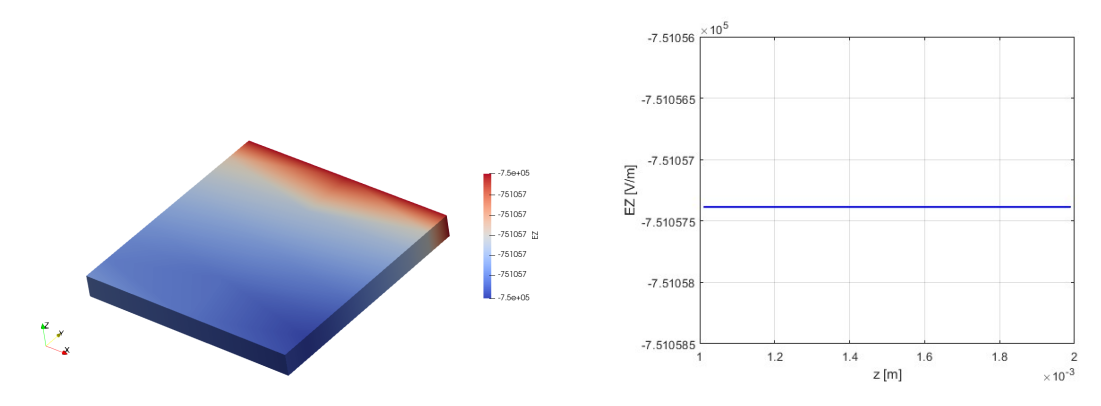


Figure 4.34: E_z

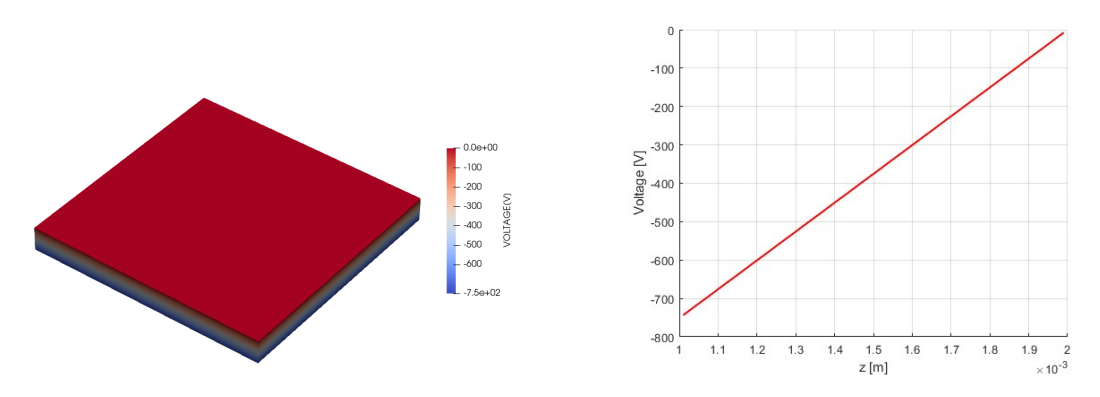


Figure 4.35: Voltage V

It can be observed that the Q4 elements, which are linear-type elements, are not able to capture the quadratic behavior of the electric potential, which is instead interpreted by these elements as linear. The electric field, on the other hand, which is expected to be linear, is captured as constant at all by these elements.

For this reason, in piezoelectric analyses, it is necessary to use Q9 elements.

Chapter 5

Capacitance

To study the composite manufacturing process using integrated piezoelectric sensors, a variable that is easily calculable is required. The capacitance, described in Section 3.2.1, is chosen as a useful variable for this purpose. We will therefore attempt to observe the capacitance trend as a function of the composite's elastic modulus.

This would provide more precise information on the composite's state during the manufacturing process, which, as we have previously seen, can lead to numerous defects.

5.1 Capacitance of a free sensor

Before studying composite manufacturing, it is necessary to calculate capacitance in a much simpler case. Suppose we have a free-standing sensor subjected to a potential difference of 100 V. Its capacitance will be calculated both analytically and by FEM to ensure the method is correct.

As seen previously, capacitance is calculated with the following formula:

$$C = \frac{Q}{V} = \frac{\oint_A D_z \, dx \, dy}{V} \tag{5.1}$$

where the eletrical displacement D is:

$$D_z = (d_{31}\sigma_1 + d_{31}\sigma_2 + d_{33}\sigma_3) + \left(\chi_{33}^t \cdot \frac{V}{t}\right)$$
 (5.2)

The d_{31}, d_{33} coefficients are the electromechanical coupling coefficients and were obtained from $\mathbf{d} = \mathbf{e} \left(\mathbf{C}^E \right)^{-1}$ that is the 3×6 electromechanical coupling matrix

In the case of a free sensor, there will be no stresses, so the formula of Capacitance is reduced to:

$$C = \int \int_{A} \left(\chi_{33}^{t} \cdot \frac{1}{t} \right) dx \, dy \tag{5.3}$$

Let's assume we have a square sensor with dimensions of 1 cm on each side and a height of 2 mm, made of PZT-4 material (the same material used in the previous evaluations). We subject this sensor to a potential difference, so we set 100 V at the bottom and 0 V at the top. The capacitance calculation is as follows:

$$C = \left(\chi_{33}^t \cdot \frac{1}{t}\right) \cdot Area = \frac{1.15 \cdot 10^{-8} F/m}{0.002m} \cdot (0.01m)^2 = 5.75 \cdot 10^{-10} F \qquad (5.4)$$

Once we have analytically calculated the capacitance we recreate this problem with a FEM model and obtain the capacitance directly from it:

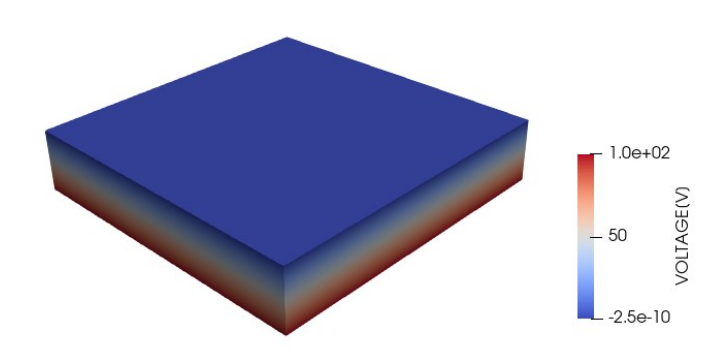


Figure 5.1: Free sensor subjected to a potential difference

Once we have obtained the electric displacement D (which in the case of a free sensor depends only on the electric field along z), we integrate it into the surface at the top of the sensor directly via the graphic visualization program and we obtain that the capacitance coincides with that calculated analytically.

$$C = 5.75 \cdot 10^{-10} F \tag{5.5}$$

5.2 Isotropic plate with integrated piezoelectric sensor

In the following section we will model a $5 \times 5 \times 2$ cm isotropic plate with the piezoelectric sensor described in the previous section integrated in the center as shown in the figures below:

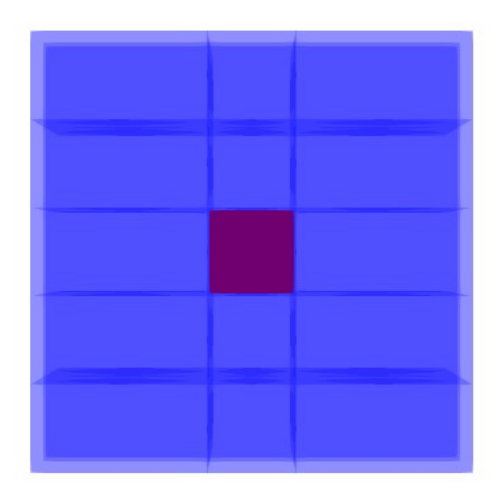


Figure 5.2: Isotropic plate with embedded piezoeletric system - Plane xy

Along the z-axis the sensor will be positioned between 1 cm and 1.2 cm:

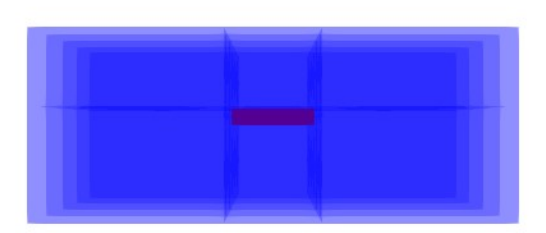


Figure 5.3: Isotropic plate with embedded piezoeletric system - Plane xz

As regards the mesh it was decided to use 5 B4 elements along the y-axis and 9 Q9 elements across the section.

The material used in the case of the sensor is the same as previously used: PZT-4 (refer to 2.1).

The properties of the isotropic plate are in Tab. (5.1) and the elastic modulus E was varied from 0.1 GPa to 320 GPa.

Properties of Isotropic Material	Value
Young's Modulus (E)	0.1 - 320 GPa
Poisson's Ratio (ν)	0.3
Density (ρ)	$2700.0\mathrm{kg/m}^3$

Table 5.1: Properties of Isotropic Material

For each value of Elastic Modulus, the capacitance observed by the embedded piezoelectric sensor was calculated:

$$C = \frac{Q}{V} = \frac{\oint_A D_z \, dx \, dy}{V} = \frac{\oint_A (d_{31}\sigma_1 + d_{31}\sigma_2 + d_{33}\sigma_3) + \left(\chi_{33}^t \cdot \frac{V}{t}\right) \, dx \, dy}{V}$$
(5.6)

The results obtained are shown below in Fig. 5.4:

The dots in the graph represent the points that were evaluated, while the red line is an interpolation of these data.

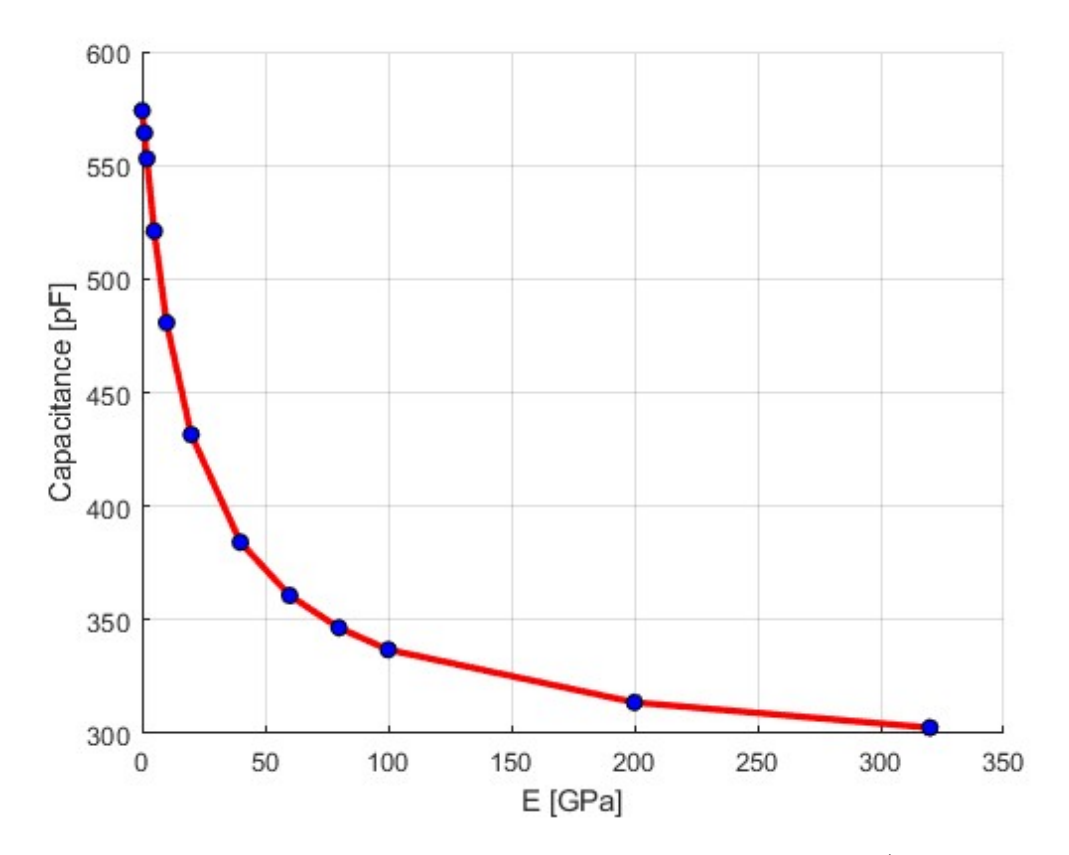


Figure 5.4: Capacitance as a function of the elastic modulus (isotropic case)

It can be observed that the capacitance value decreases very rapidly as the elastic modulus of the isotropic plate housing the sensor increases for low elastic moduli. As the elastic modulus increases, the capacitance no longer decreases and settles around a value of 300 pF.

5.3 Laminated composite with embedded piezoelectric sensor

In the following section, the behavior of a piezoelectric sensor integrated into a symmetric composite laminate (10 layers) during the manufacturing process is analyzed. To do this, the 5x5x0.2 cm composite is modeled with 10 layers (each 0.02 cm thick) of orthotropic material with 0-90-0-90-0-90-0 orientation.

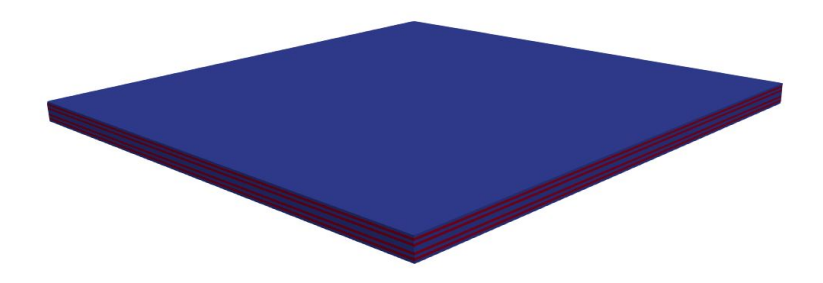


Figure 5.5: Laminated Composite

For the mechanical characteristics of the orthotropic material, present with 2 different orientations in the composite, the values of Elastic Modulus E, Poisson ν and Shear Stress G in the 3 directions at different times during the manufacturing process with a Curie temperature of 180°C are obtained from the literature (in particular from paper [15]).

Fig. 5.6 shows the trend of the Degree of Cure and the Elastic Moduli as a function of time with the data extrapolated from paper [15]).

Tab.5.2 instead shows the DOC values with the respective characteristics of the orthotropic material in which it was decided to calculate the capacitance for a study of its trend as a function of the DOC.

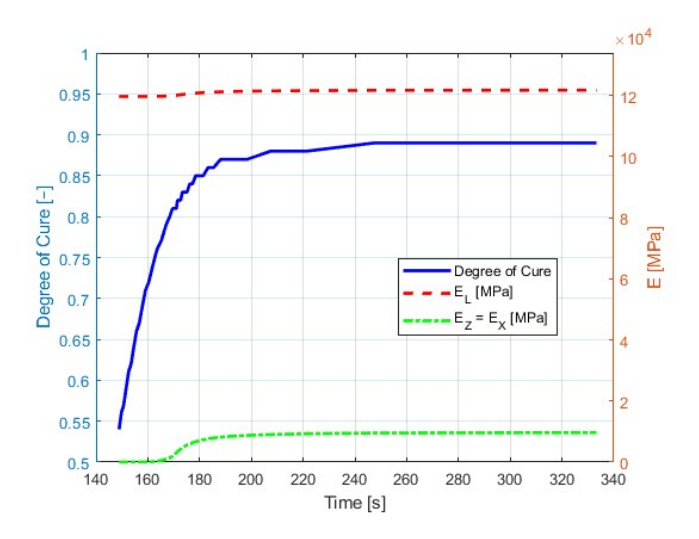


Figure 5.6: Curing Cycle

DOC T [°C]	0.54 168.88	0.59 171.60	0.67 176.71	0.74 180.00	0.80 180.00	0.85 180.00	0.89 20.00
E_1 [GPa]	119.70	119.70	119.70	119.71	119.85	120.77	121.75
E_2 [MPa]	0.25	1.13	14.56	144.62	1429.67	6689.40	9674.51
E_3 [MPa]	0.25	1.13	14.56	144.62	1429.67	6689.40	9674.51
$ u_{12}$	0.329	0.329	0.329	0.329	0.324	0.297	0.269
$ u_{13}$	0.329	0.329	0.329	0.329	0.324	0.297	0.269
$ u_{23}$	0.999	0.999	0.999	0.991	0.911	0.600	0.441
G_{12} [MPa]	0.06	0.28	3.64	36.50	393.25	2763.29	5163.91
G_{13} [MPa]	0.06	0.28	3.64	36.50	393.25	2763.29	5163.91
G_{23} [MPa]	0.06	0.28	3.64	36.32	373.98	2091.03	3357.54

Table 5.2: Material properties for different DOC and temperatures.

At the center of the laminate, in the sixth layer, an embedded piezoelectric sensor with dimensions 1 x 1 x 0.02 cm is inserted.



Figure 5.7: Piezoeletric Sensor embedded in laminated composite

For the piezoelectric material, it was decided to carry out various analyses with 4 different types of piezoelectric materials: PZT-4, PZT-5H, PZT-5A and PZT-8. The mechanical, piezoelectric and dielectric characteristics are reported in the Tab 2.1.

As a starting point, the capacitance of the sensor is calculated in free-standing conditions, meaning what, without any mechanical stress acting on it. These values will be used for comparison later.

$$C = \left(\chi_{33}^t \cdot \frac{1}{t}\right) \cdot Area \tag{5.7}$$

	PZT-4	PZT-5H	PZT-5A	PZT-8
Capacitance [pF]	5750	6650	7500	4450

Table 5.3: Capacitance of 4 sensors in free conditions: PZT-4, PZT-5H, PZT-5A and PZT-8

5.3.1 Capacitance with Permittivity fixed

At this point, various analyses are performed at different degrees of cure on the composite using the three types of embedded piezoelectric sensors. The capacitance is calculated as a function of the DOC cure degree using the following formula, keeping the permittivity values shown in the table fixed:

$$C = \frac{\oint_A D_z \, dx \, dy}{V} = \frac{\oint_A \left(d_{31}\sigma_1 + d_{31}\sigma_2 + d_{33}\sigma_3 \right) + \left(\chi_{33}^t \cdot \frac{V}{t} \right) \, dx \, dy}{V} \tag{5.8}$$

The results are shown in Fig. 5.8.

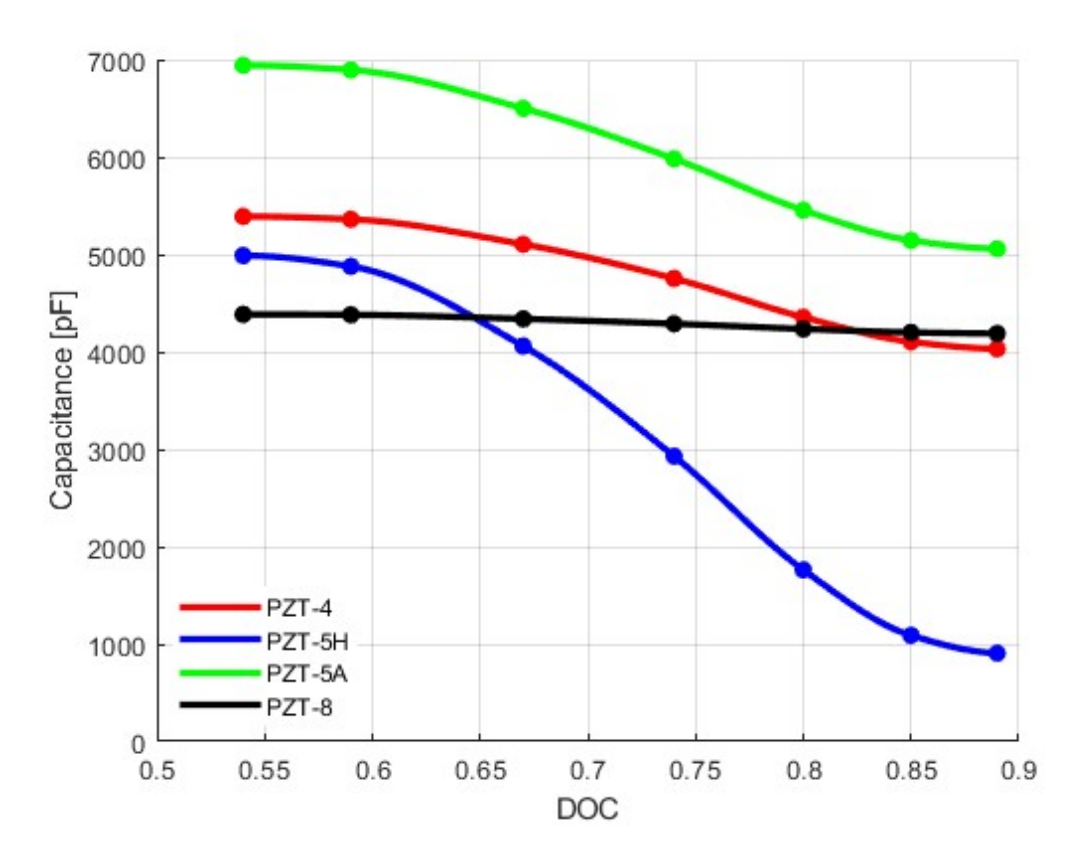


Figure 5.8: Capacitance of PZT-4, PZT-5H, PZT-5A and PZT-8 as a function of the Degree of Cure

The results show that at a fixed permittivity, capacitance is only affected by mechanical stress in all three directions, which causes capacitance to decrease. This occurs because, as the degree of cure increases, the generation of mechanical stresses due to the hardening of the composite decreases. It is noted that the PZT-8 has a rather stable capacitance trend, probably due both to the fact that it has a stable permittivity as a function of temperature and because, having lower mechanical couplings, it is less sensitive to mechanical stress.

5.3.2 Capacitance with Permittivity as a function of the Temperature

In this section, we decided to investigate the role of permittivity within the capacitance formula. It is known that permittivity increases near the Curie temperature of the respective piezoelectric material.

Previously, the permittivity of the 4 piezoelectric materials was calculated as a function of temperature (2.9). It was observed that the permittivity of PZT-5H explodes near 180°C, while PZT-5H and PZT-5A showed a similar permittivity trend which probably suggests that they have a higher curie temperature than PZT-5H.

At this point, the analyses for calculating the capacitance are performed again, this time with the permittivity as a function of temperature:

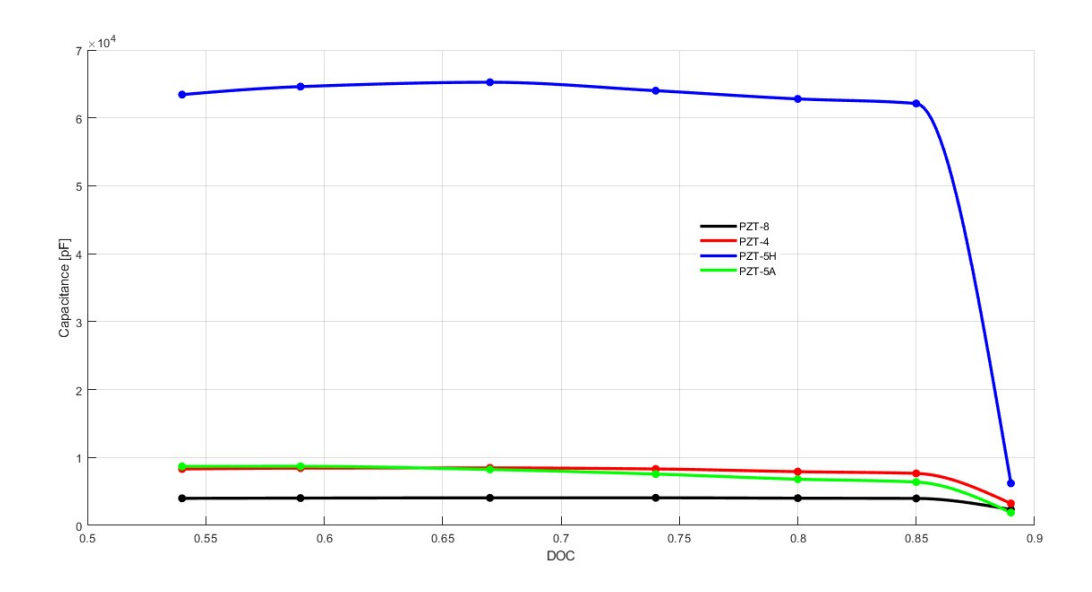


Figure 5.9: Capacitance of PZT-4, PZT-5H, PZT-5A and PZT-8 with permittivity variable as a function of the Temperature

As expected, it is observed in Fig. 5.9 that the capacitance calculated with

the permittivity as a function of temperature is significantly affected by this factor. Although the capacitance trend calculated with a fixed permittivity was very similar between the 4 sensor types, in this case it is observed that the capacitance trend is strongly influenced by the permittivity trend as a function of temperature. This is demonstrated by the fact that the PZT-5H has a capacitance that reaches an order of magnitude higher than the other two and is due to the fact that the permittivity, near the Curie temperature of the PZT-5H, increases significantly.

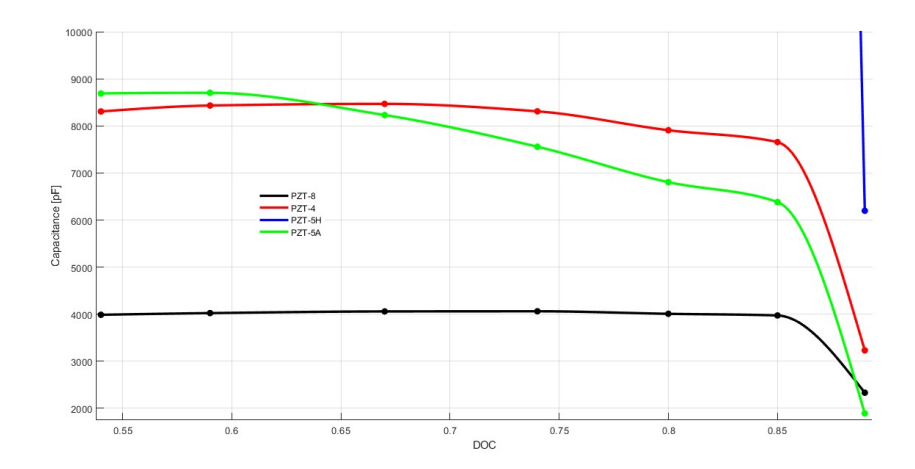


Figure 5.10: Zoom of Capacitance of PZT-4, PZT-5H, PZT-5A and PZT-8 with permittivity variable as a function of the Temperature

The capacitance trend of PZT-4 and PZT-5H is quite similar. It can be observed that both are slightly variable when compared to PZT-8, which exhibits a stable trend. The capacitance trend of PZT-8 is due both to the fact that, from a thermal point of view, the permittivity of this material is not affected by any variation, but also to the fact that, having a lower mechanical coupling (refer to Tab. 2.1), it is less affected by variations in mechanical stress and is therefore less sensitive than PZT-4 and PZT-5A.

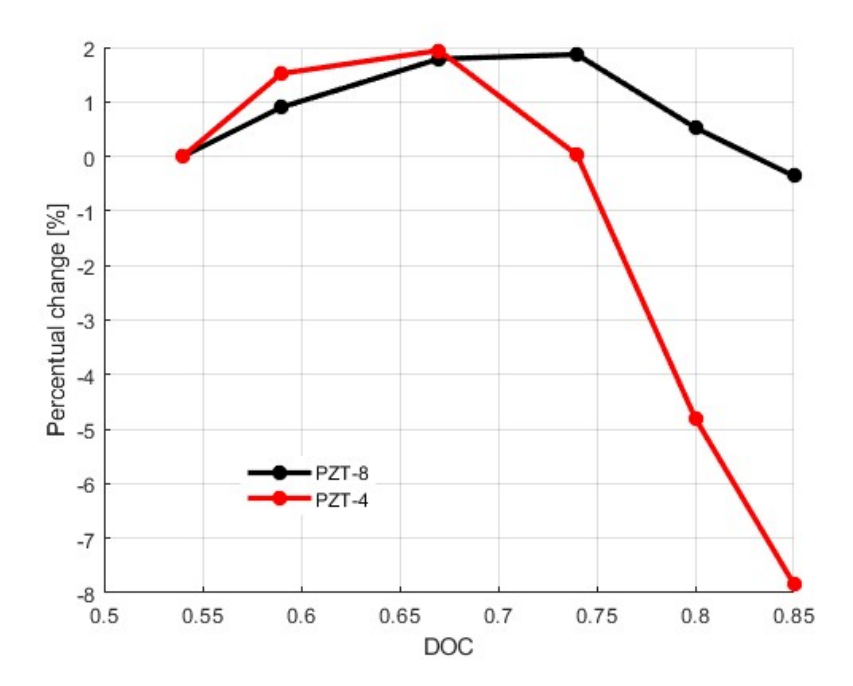


Figure 5.11: Percentage change calculated with respect to the first real capacitance value

Fig. 5.11 shows a comparison between the percentage change in capacitance with respect to the first calculated value both in the case of the PZT-8 and in the case of the PZT-4.

It can be observed that the capacitance calculated with the PZT-8 sensor is much less variable than that calculated with the PZT-4 sensor, demonstrating what was said previously.

5.3.3 Comparison between PZT-4 and PZT-5A

In this section, we choose to make a more in-depth comparison between PZT-4 and PZT-5A. These two materials were chosen because the results reported previously showed that they represent the right compromise between good sensitivity to mechanical stress and a permittivity that is little affected by the temperature at which the curing process is carried out, thanks to a high Curie temperature.

Comparison of the 3 capacitances: analytical, with fixed permittivity and with permittivity as a function of temperature

First, we compare the capacitance trend as a function of DOC. The capacitances considered are: the analytical capacitance, the capacitance calculated with a fixed permittivity, and the capacitance calculated with a variable permittivity as a function of temperature.

The analysis shows in Fig. 5.12 that, in the case of the PZT-5A, the three capacitance trends (analytic, fixed permittivity, and variable permittivity) generate very similar patterns. This is attributable to the greater thermal stability of the permittivity of the PZT-5A, which undergoes smaller variations with temperature than the PZT-4. In contrast, the PZT-4 exhibits a greater dependence of its permittivity on temperature, which significantly affects the measured capacitance, making the three models very different.

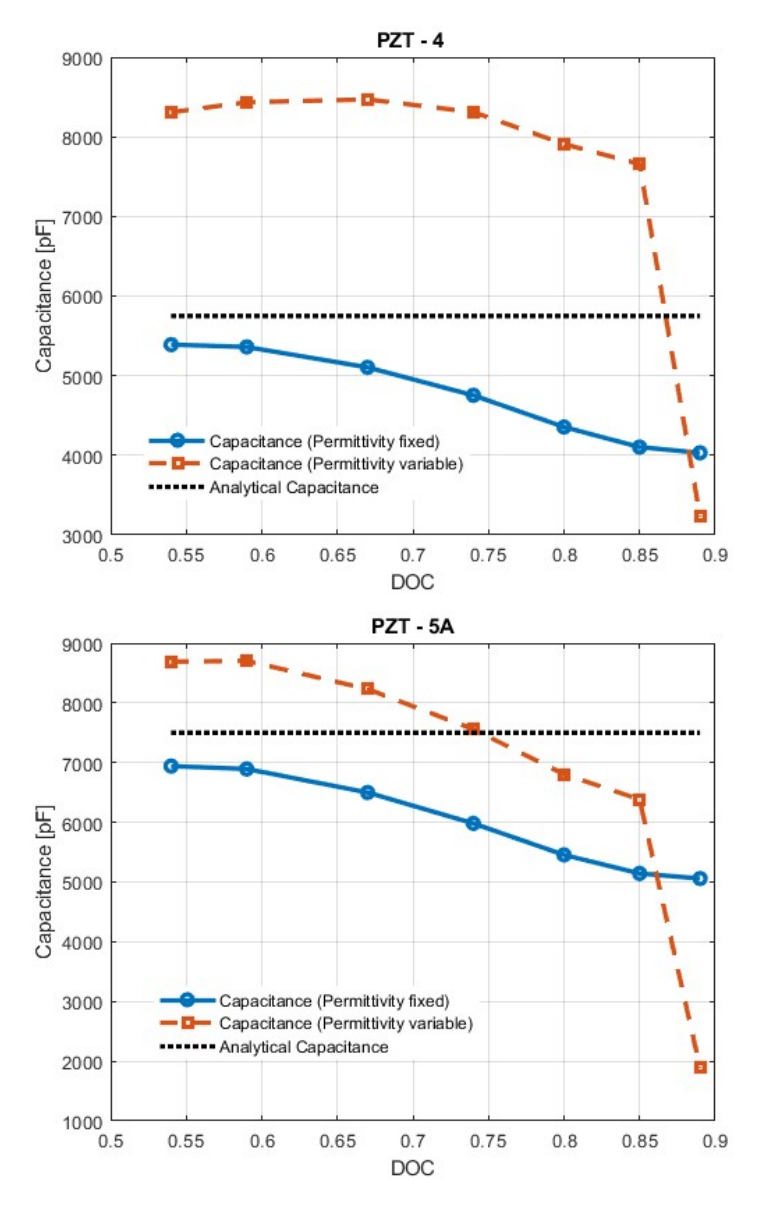


Figure 5.12: Comparison of the 3 capacitances: analytical, with fixed permittivity and with permittivity as a function of temperature

Percentage change calculated with respect to the first real capacitance value

Secondly, it was decided to compare the trend of the percentage variation calculated with respect to the first capacitance value measured in the two cases.

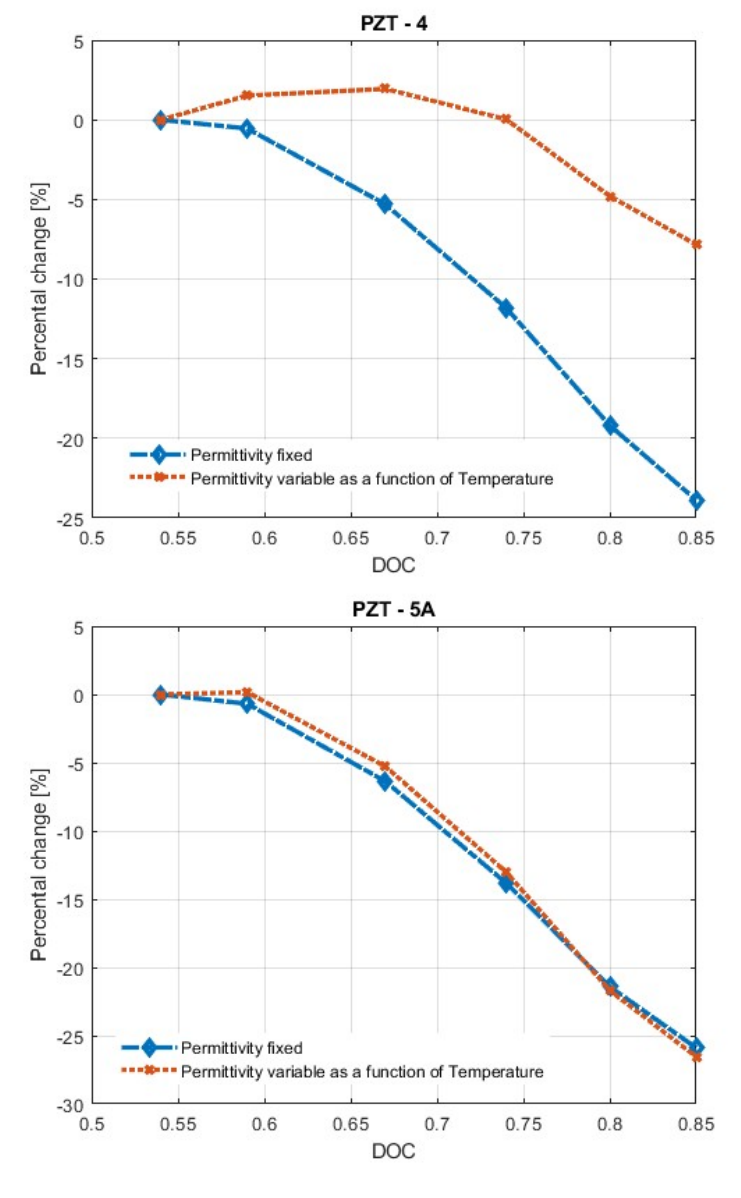


Figure 5.13: Percentage change calculated with respect to the first real capacitance value

The fact that, in the case of PZT-5A, the percentage change in capacitance is similar with both fixed and variable permittivity suggests that the permittivity of PZT-5A is more stable than the permittivity of PZT-4. This is demonstrated in Fig. X. This implies that the influence of temperature on permittivity in the case of PZT-5A is less than that of other piezoelectric materials (such as PZT-4), and therefore the measured capacitance is more sensitive to mechanical stress rather than thermal variations.

Conversely, in the case of PZT-4, the marked difference between the two curves indicates that the permittivity of the material varies significantly with temperature. This makes it more difficult to interpret the change in capacitance as an effect of the composite alone, since a significant portion of the observed variation is due to the thermal behavior of the sensor itself.

From this analysis it emerges that the PZT-5A represents a more robust choice for capacitance monitoring applications during the curing phase, as it allows to better isolate the effect of the composite hosting the piezoelectric sensor.

Comparison of the capacitance obtained in the case of lower Curing Temperatures

For a further comparison of the performances of PZT-4 and PZT-5A, it was decided to calculate the trend of the capacitance as a function of the DOC in the case of a cure with a maximum temperature lower than the previous one. This is the case for composites used in sectors requiring simpler processing, lower costs, or where high temperatures are not compatible with the process.

In the first case the maximum curing temperature is 150 $^{\circ}$ C and the holding time is 800 minutes:

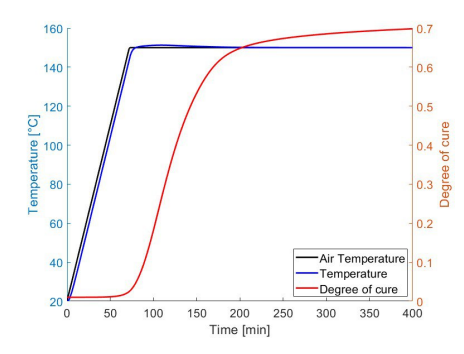


Figure 5.14: Maximum Curing Temperature: 150°C

In the second case the maximum curing temperature is 165 $^{\circ}$ C and the holding time is 600 min.

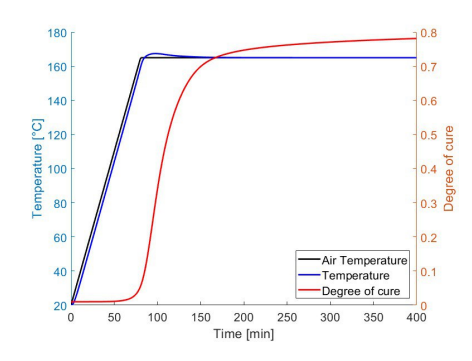


Figure 5.15: Maximum Curing Temperature: 165°C

The capacitance at various DOCs is then calculated in the two cases. The following Fig. 5.16 shows the different capacitance trends as a function of DOC, also compared with the capacitance trend in the case of maximum curing temperature at 180°C (the previous case).

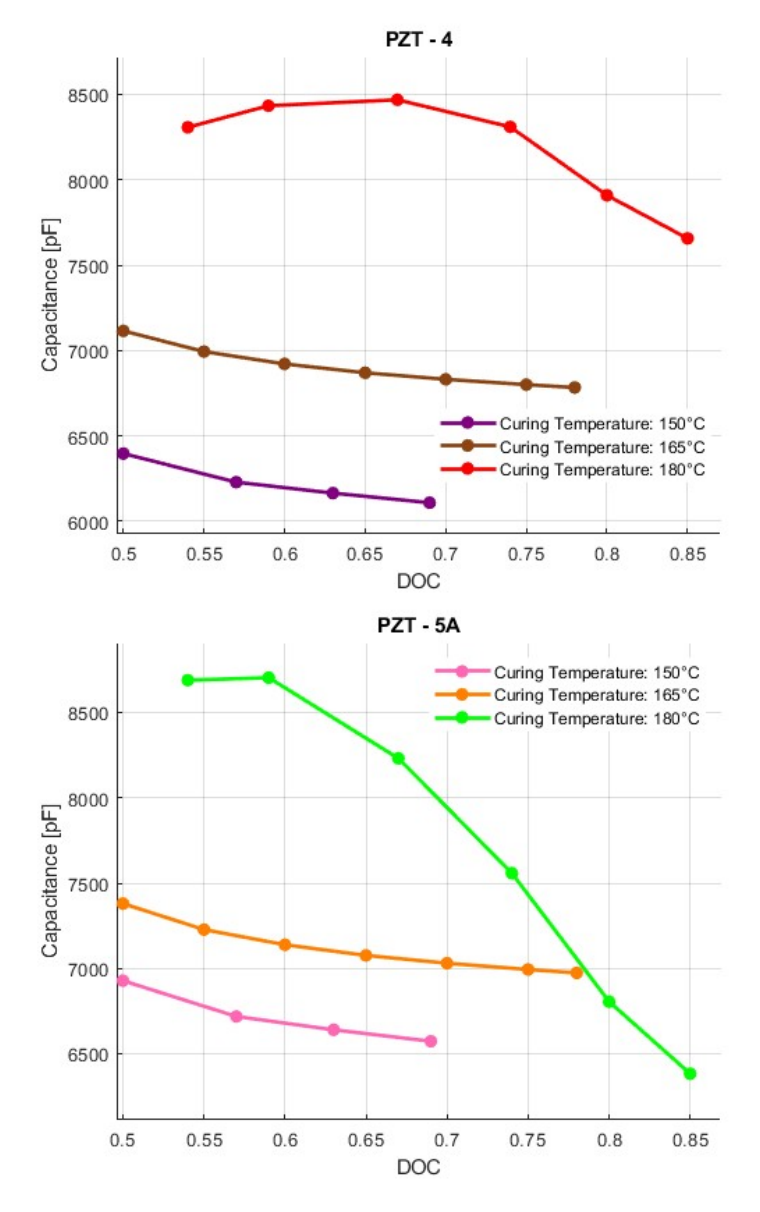


Figure 5.16: Capacitance trend as a function of DOC in the 3 cases at different maximum curing temperatures

In all three cases, the capacitance was calculated with the permittivity varying as a function of temperature.

In the case of curing process at 150°C and 165°C, both sensors (PZT-4 and PZT-5A) show a higher capacitance stability as a function of DOC, probably because at those temperatures the sensors undergo less thermal stress and also less mechanical stress.

With the curing process at 180°C, the composite is subjected to greater stress and more marked relaxation phenomena, which is reflected in a more variable capacitance.

Chapter 6

Conclusions

This thesis therefore sought to analyze the capacitance behavior measured by the piezoelectric sensor integrated within a composite structure during the manufacturing process. To achieve this, however, we began by using the Mul2polito code for very simple, purely mechanical problems such as those analyzed in Assessment 1 (the doubly fixed beam loaded at the center) and Assessment 2 (the multilayer beam loaded at the ends). After this initial part, we moved on to a more complex electromechanical problem in Assessment 3 (isotropic beam + piezoelectric patch for both the actuator and sensor cases). At this point, the capacitance value of a piezoelectric sensor was calculated in free-standing conditions. Subsequently, the capacitance behavior of a piezoelectric sensor embedded in a plate of isotropic material with increasing elastic modulus was analyzed. Finally, the capacitance behavior of the piezoelectric sensor embedded in a multilayer composite laminate was analyzed during the manufacturing process. Finally, the literature was searched for an ideal piezoelectric material for this type of operation at very high temperatures during the composite curing process.

The most important conclusions that emerged from this study are:

- Significant differences are observed between the various models used to represent the beam's behavior. In particular, Taylor Expansion (TE) models provide a more uniform representation of the cross-section, but simplify the distribution of strains and stresses. Lagrange Expansion (LE) models, on the other hand, allow for a more precise description of local phenomena, thanks to their ability to better capture the actual deformation of the cross-section. Lower-order TE models (TE-1, TE 0, TE 1) are unable to accurately represent the cross-section deformation, while starting from TE 2, results comparable to those of LE models are obtained. Increasing the expansion order (up to TE 4) further improves accuracy, especially at the center of the cross-section, although discrepancies remain at the ends. LE 2 and LE 3 models show good convergence towards the correct solution, with LE 3 offering the greatest accuracy but requiring a high number of degrees of freedom.
- Regarding the **elements used on the cross-section**, it was observed that in the case of piezoelectric analyses, it is necessary to use Q9 elements. In Assessment 3, in fact, it was agreed that the Q4 elements, which are linear, are not able to capture the quadratic behavior of the electric potential, which is instead interpreted by these elements as linear. The electric field, on the other hand, which is expected to be linear, is captured as constant at all by these elements.
- From the study of the **Isotropic plate** with the integrated piezoelectric sensor, it was found that the capacitance shows an exponential decrease behavior, with a rapid initial increase followed by a progressive stabilization

as the Elastic Modulus of the isotropic material hosting the piezoelectric sensor increases. This is likely due to the fact that as the elastic modulus E of the plate increases, the structure becomes more rigid and offers greater resistance to the deformation imposed by the sensor. Consequently, the mechanical deformations in the piezoelectric sensor decrease. This reduces the change in electrical charge generated by the piezoelectric deformation, also influencing the piezoelectric sensor's capacitance response.

• Studying the Composite laminate during its curing process, a decreasing behavior of capacitance is observed as a function of the Degree of Cure if the permittivity value is considered fixed (not as a function of temperature). In this case, despite the comparison between different piezoelectric sensors (PZT-4, PZT-5H, PZT-5A and PZT-8), the capacitance trend is quite similar. However, considering permittivity as a function of temperature, which varies from sensor to sensor, it is observed that the capacitance of the piezoelectric sensor has a quite different trend based on the type of piezoelectric material used. This demonstrates how the choice of piezoelectric sensor material is of fundamental importance. It was noted that in the three piezoelectric materials analyzed, the permittivity has an increasing trend around the composite's curing temperature. This is due to the proximity to the respective Curie temperature of each piezoelectric material, the point at which permittivity explodes. The piezoelectric material selected for this type of composite monitoring during the polymerization process must have both a permittivity that is as constant as possible at the polymerization temperature (i.e., a high Curie temperature) and high sensitivity to mechanical stress.

It has been shown that PZT-5H is not the right material for this type

of monitoring due to its low Curie temperature and, consequently, a permittivity that increases exponentially around 180°C, the temperature of interest for the composite curing process.

It has been observed that PZT-8, despite its constant permittivity, does not possess great mechanical sensitivity due to its low mechanical coupling. The final comparison between PZT-4 and PZT-5A led to the conclusion that PZT-5A is more suitable for this type of monitoring because it has been shown to be less affected by permittivity as a function of temperature in the capacitance calculation. PZT-5A therefore has a greater sensitivity to mechanical stress than PZT-4 and this allows us to understand more clearly what happens during the curing process in the composite laminate that houses the sensor.

• Finally, it was observed that the capacitance of composites with lower curing temperatures is less variable than that of those with higher curing temperatures. This would therefore make the piezoelectric materials analyzed in this work more suitable as integrated sensors for composites with medium curing temperatures, and therefore not high-performance.

Bibliography

- [1] G. Li E. Carrera, E. Zappino. Analysis of beams with piezo-patches by node-dependent kinematic fem models. *Journal of Intelligent Material Systems and Structures*, 2017.
- [2] E. Zappino. The slides from the course: " aerospace technologies". *Politec-nico di Torino*, 2024/2025.
- [3] Sara Biamino. The slides from the course: "materials for aerospace applications". *Politecnico di Torino*, 2024/2025.
- [4] Mahto D. Kumar S. Recent trends in industrial and other engineering applications of non destructive testing: a review. *Int J Sci Eng Res*, 2013.
- [5] Z. Aboura Y. Meyer K. Khellil R. Lachat C. Tuloup, W. Harizi. On the use of in-situ piezoelectric sensors for the manufacturing and structural health monitoring of polymer-matrix composites: A literature review. www.elsevier.com/locate/compstruct, 2019.
- [6] Croxford AJ Bond IP Chilles JS, Koutsomitopoulou AF. Monitoring cure and detecting damage in composites with inductively coupled embedded sensors. *Compos Sci Technol*, 2016.

- [7] Zappino E. Carrera E. Advanced modeling of embedded piezo-electric transducers for the health-monitoring of layered structures. 2020.
- [8] D. Scano E. Zappino, E. Carrera. The slides: "advanced tailored kinematic models for multi-field analysis of laminated structures". XI ECCOMAS Thematic Conference on Smart Structures and Materials SMART 2025, Linz, Austria, 2025.
- [9] Erasmo Carrera Walid Harizi Jamal Najd, Enrico Zappino and Zoheir Aboura. A variable kinematic model for the prediction of capacitance variations in embedded pzt sensors. *Journal of Intelligent Material Systems* and Structures, 2017.
- [10] Hua Tian Jiyang Wang Wenwu Cao Yang Zhang, Liguo Tang and Zhongwu Zhang. Determination of temperature dependence of full matrix material constants of pzt-8 piezoceramics using only one sample. *Journal of Alloys and Compounds*, 714:20–25, 2017. doi: 10.1016/j.jallcom.2017.04.124. URL https://doi.org/10.1016/j.jallcom.2017.04.124.
- [11] Boston Piezo-Optics. Ceramic materials pzt (material data for pzt ceramics). URL https://bostonpiezooptics.com/ceramic-materials-pzt.
- [12] Virginia Matthew W. Hooker Lockheed Martin Engineering Sciences Co., Hampton. Properties of pzt-based piezoelectric ceramics between-150 and 250°c. Langley Research Center, 1998.
- [13] E. Zappino M. Petrolo E. Carrera, M. Cinefra. Finite element analysis of structures through unified formulation. *Politecnico di Torino*, 2014.
- [14] G. Li E. Carrera, E. Zappino. Finite element models with node-dependent kinematics for the analysis of composite beam structures. *MUL2 Group*,

BIBLIOGRAPHY

Department of Mechanical and Aerospace Engineering, Politecnico di Torino, 2017.

[15] M. Petrolo R. Vaziri E. Carrera A. Poursartip E. Zappinoa, N. Zobeiry. Analysis of process-induced deformations and residual stresses in curved composite parts considering transverse shear stress and thickness stretching. www.elsevier.com/locate/compstruct, 2020.